aerospace

MDPI

Article

Pose-Constrained Control of Proximity Maneuvering for Tracking and Observing Noncooperative Targets with Unknown Acceleration

Mingyue Zheng [1], Yulin Zhang [1], Xun Wang [2] and Li Fan [1,3,*]

[1] College of Control Science and Engineering, Zhejiang University, Hangzhou 310027, China
[2] Department of Aerospace Science and Technology, Space Engineering University, Beijing 101400, China
[3] Huzhou Institute of Zhejiang University, Huzhou 313002, China
* Correspondence: fanli77@zju.edu.cn

Abstract: This paper proposes a pose control scheme of for proximity maneuvering for tracking and observing noncooperative targets with unknown acceleration, which is an important prerequisite for on-orbit operations in space. It mainly consists of a finite-time extended state observer and constraint processing procedures. Firstly, relative pose-coupled kinematics and dynamics models with unknown integrated disturbances are established based on dual quaternion representations. Then, a finite-time extended state observer is designed using the super-twisting algorithm to estimate the integrated disturbances. Both observation field of view and collision avoidance pose-constrained models are constructed to ensure that the service spacecraft continuously and safely observes the target during proximity maneuvering. And the constraint models are further incorporated into the design of artificial potential function with a unique minimum. After that, the proportional–derivative-like pose-constrained tracking control law is proposed based on the estimated disturbances and the gradient of the artificial potential function. Finally, the effectiveness of the control scheme is verified through numerical simulations.

Keywords: proximity maneuver; noncooperative target tracking; extended state observer; disturbance suppression; collision avoidance; artificial potential function

Citation: Zheng, M.; Zhang, Y.; Wang, X.; Fan, L. Pose-Constrained Control of Proximity Maneuvering for Tracking and Observing Noncooperative Targets with Unknown Acceleration. *Aerospace* **2024**, *11*, 828. https://doi.org/10.3390/aerospace11100828

Academic Editors: Fanghua Jiang

Received: 25 August 2024
Revised: 29 September 2024
Accepted: 7 October 2024
Published: 9 October 2024

1. Introduction

The proximity maneuvering of spacecraft is generally defined as the operation of one orbiting spacecraft moving in close proximity to another orbiting object [1], which is an important prerequisite for conducting on-orbit servicing [2]. Active controlled proximity maneuvering builds suitable relative motions for on-orbit operations [3], such as inspection, capturing, refueling, facility maintenance, and debris removal. The control technology for spacecraft proximity maneuvering is key to guaranteeing the safety, efficiency, and precision of the approach process, and has attracted attention in both theoretical research and engineering design. Target spacecraft are generally categorized into cooperative and noncooperative types based on the degree of their cooperation with the chaser spacecraft [4]. Maneuver control for tracking cooperative targets in space has made significant progress and is gradually maturing from theories to ground-based hardware-in-the-loop simulation validation [5,6], and to on-orbit applications [7,8]. However, compared with cooperative targets, various types of information about noncooperative objects are not easy to obtain, making it difficult to directly apply tracking methods and techniques from cooperative targets to noncooperative objects. At present, tracking noncooperative targets through proximity maneuvering is still challenging and unsolved.

The main reasons for the significant difficulty in tracking noncooperative targets in space include four aspects. (1) Noncooperative targets will not send pose information to the chaser spacecraft in the absence of communication between the two participating

entities, resulting in a lack of the relative motion state required for tracking. (2) There exists strong coupling between position translation and attitude rotation. Efficient adjustment and control of the relative pose are required to ensure spacecraft safety and meet task constraints, especially in cases where the two spacecraft are close and their volumes are large [9]. (3) The noncooperative target itself may generate unknown pose maneuver accelerations due to functional anomalies, as well as the unknown disturbance forces and moments always existing in space. They will lead to a reduction in tracking accuracy. (4) Proximity maneuvering is not just about flying near a target, but also performing certain specific tasks such as observation, docking, and refueling. The actuators installed on the chaser spacecraft also place some constraints on their relative pose.

In order to deal with the above difficulties, scholars and engineers have conducted relevant studies considering one or several aspects of them. Acquiring relative pose and motion states is relatively independent from the other three aspects. With measurement data from laser, infrared, and visible vision [10,11], researchers have developed various estimation algorithms to obtain the relative pose, the angular and linear velocity of noncooperative objects [12–14], specifically including convolutional neural network-based monocular pose estimation [15], the simultaneous estimation of pose and shape [16], consecutive point cloud-based estimation [17,18], template matching with sparse point clouds [19], and Kalman filtering [20]. The coupling of rotation and translation comes from the close correlation between the force/torque acting on the spacecraft and its pose. Many efforts have been devoted to solving this problem. Subbarao and Welsh [21] proposed an attitude-synchronization approach combined with relative position tracking to keep the docking components of two spacecraft in a suitable orientation as the relative distance decreases. Alex Pothen et al. [22] designed a pose tracking controller based on the Udwadia–Kalaba equation for spacecraft proximity operations. Di Mauro et al. [23] proposed a differential-algebra based solution algorithm to deal with the relative position tracking and attitude synchronization problem, and performed hardware-in-the-loop experimental validation on the ground. The negative effects of uncertain disturbance in proximity maneuvering have also attracted some attention, and there are two main types of solutions for this problem. One is to directly design a robust controller, and another is to design a feedback controller with an observer. Sun and Huo [24] combined backstepping and adaptive control to, respectively, design position and attitude controllers considering parameter uncertainties and unknown external disturbances for chaser spacecraft approaching a noncooperative tumbling target. Gui and de Ruiter [25] designed a concurrent position and attitude tracking law on a novel hybrid dual quaternion integral sliding mode that incorporates hysteretic switching, making tracking errors globally finite-time-convergent in the presence of actuator faults, mass and inertia uncertainties, and unknown external disturbances. Wang et al. [26] developed an adaptive robust fault-tolerant control scheme for spacecraft proximity operations. The tracking accuracy can also be effectively improved by compensating for disturbances, which are usually estimated by a disturbance observer or an extended state observer (ESO). Lee [27] proposed a nonlinear disturbance observer for estimating environmental disturbances, which is used as a feedforward term in control to enhance disturbance attenuation ability and robustness performance. Fu et al. [28] developed a robust nonlinear model predictive control scheme with prescribed performance based on a fixed-time neural network disturbance observer for on-orbit inspection maneuvering. Dong et al. [29] designed a smooth six-degree-of-freedom (6-DOF) observer based on the dual quaternion to estimate dual-angular velocity incorporating linear and angular velocity, and further designed a feedback control law using the estimated states. Sun et al. [30] designed an ESO to estimate and compensate for total uncertainty in relative dynamics. The fixed-/finite-time ESO has the advantage of fast convergence, and can be combined with the terminal sliding-mode control or backstepping method for tracking, leading to a good dynamic response and low steady-state error [31,32]. Additional relative pose constraints resulting from collision avoidance or specific missions are also important topics in proximity maneuver control. Wang et al. [33,34] established appearance envelopes

of spacecraft, which were used to formulate optimization constraints in model predictive control to achieve proximity collision avoidance in flight. Lee et al. [35] proposed optimal tracking control based on penalty function for real-time collision avoidance maneuvering during spacecraft proximity operations. Li et al. [36] divided the approach corridor into two phases according to the safety and mission requirements of spacecraft approach maneuvering, and then constructed performance functions for designing control laws. Wang et al. [37] proposed an equal-collision-probability-curve method for safe proximity maneuvering to reduce collision risk and save on fuel consumption. Ikeya et al. [38] presented a learning-based reference governor to enforce mission constraints through learning, which reduced modeling requirements.

At present, the simultaneous coordinated control of relative position and attitude is still the focus of researchers' attention, and spacecraft safety during relative motion, as well as the specific mission requirements, are also widely considered. Most studies are based on the assumption that the angular and linear acceleration of the target is known, and directly use acceleration as an offset term in control law design [2,39,40]. However, this assumption is feasible for cooperative targets but infeasible for noncooperative objects. It is incredibly difficult to obtain the acceleration of noncooperative targets, which will result in some items of their control laws being unable to be solved; thus, instructions for actuators cannot be formed in practice scenarios. This paper investigates the pose control of service spacecraft during their continuously visual observation for noncooperative targets through proximity maneuvering. The main contributions of this paper include two aspects. An ESO based on the super-twisting algorithm (STA) is designed to estimate unknown disturbance terms, which are used in the control law to suppress their negative effects. Moreover, observation and collision avoidance constraint models are established on a dual quaternion to further design an artificial potential function (APF) with only one minimum. The control law is developed on the basis of estimated disturbances and the APF, which can enable the continuous observation of the target during the proximity maneuver and, ultimately, stable tracking.

The remaining parts of this paper are organized as follows. Section 2 provides the basics about quaternions and dual quaternions. Section 3 derives the relative pose kinematics and dynamics equations with unknown integrated disturbances. Section 4 formulates the STA-based ESO for the disturbance estimation. Section 5 establishes field-of-view (FOV) and collision avoidance constraint models using the relative pose dual quaternions. Section 6 presents the proximity maneuver control law based on estimated disturbances and the APF method. Section 7 establishes unknown-disturbance models and conducts numerical simulations for the verification of the control law. Section 8 gives our conclusions.

2. Quaternions and Dual Quaternions

Quaternions were first introduced by Hamilton [41] and have advantages in attitude representations, especially in effectively avoiding singularities. Dual quaternions were introduced by Clifford [42] based on quaternions and can be used as pose representations. The definition of a quaternion q is as follows:

$$q = q_0 + q_1 i + q_2 j + q_3 k \tag{1}$$

where $q_0, q_1, q_2, q_3 \in \mathbb{R}$, and the operation rules between i, j, and k are $i^2 = j^2 = k^2 = -1$, $ij = -ji = k$, $jk = -kj = i$, and $ki = -ik = j$. A quaternion can also be written in the ordered pair of a scalar and a vector:

$$q = (q_0, \vec{q}\,) \tag{2}$$

where q_0 and $\vec{q} = (q_1, q_2, q_3)^{\mathrm{T}} \in \mathbb{R}^3$ are referred to as the scalar part and vector part of the quaternion q, respectively. And q is also treated as a real scalar in some situations if $\vec{q}$ is the zero vector in three dimensions. The definition of a dual quaternion $\boldsymbol{q}$ is as follows:

$$\boldsymbol{q} = q_r + \epsilon q_d \tag{3}$$

where ϵ is a dual unit defined by $\epsilon \neq 0$ and $\epsilon^2 = 0$, and q_r and q_d are quaternions, which are referred to as the real part and dual part of $\boldsymbol{q}$, respectively. The detailed operation rules of quaternions and dual quaternions can be found in [43]. In order to make the subsequent content easy to understand, this section only lists some of them and other unique operation rules defined in this paper as follows:

- Conjugation: $q^* = (q_0, -\vec{q})$ and $\boldsymbol{q}^* = q_r^* + \epsilon q_d^*$.
- Matrix generation: $[q] = \begin{bmatrix} q_0 & -\vec{q}^{\mathrm{T}} \\ \vec{q} & q_0 \mathrm{I}_{3\times 3} + [\vec{q}] \end{bmatrix}$ and $[\boldsymbol{q}] = \begin{bmatrix} [q_r] & 0_{4\times 4} \\ [q_d] & [q_r] \end{bmatrix}$, where $[\vec{q}] = \begin{bmatrix} 0 & -q_3 & q_2 \\ q_3 & 0 & -q_1 \\ -q_2 & q_1 & 0 \end{bmatrix}$.
- Dot product: $p \cdot q = (p_0 \cdot q_0 + \vec{p} \cdot \vec{q}, \vec{0}_{3\times 1}) = p_0 \cdot q_0 + \vec{p} \cdot \vec{q}$.
- Circle product: $\boldsymbol{p} \circ \boldsymbol{q} = p_r \cdot q_r + p_d \cdot q_d$.
- Scalar part: $\mathrm{sca}(q) = (q_0, \vec{0}_{3\times 1})$ and $\mathrm{sca}(\boldsymbol{q}) = \mathrm{sca}(q_r) + \epsilon \mathrm{sca}(q_d)$.
- Vector part: $\mathrm{vec}(q) = (0, \vec{q})$ and $\mathrm{vec}(\boldsymbol{q}) = \mathrm{vec}(q_r) + \epsilon \mathrm{vec}(q_d)$.
- Sign extraction: $\mathrm{sign}(q) = (\mathrm{sgn}(q_0), \mathrm{sgn}(\vec{q}))$ and $\mathrm{sign}(\boldsymbol{q}) = \mathrm{sign}(q_r) + \epsilon \mathrm{sign}(q_d)$, where $\mathrm{sgn}(\cdot)$ is a sign function and $\mathrm{sgn}(\vec{q}) = (\mathrm{sgn}(q_1), \mathrm{sgn}(q_2), \mathrm{sgn}(q_3))^{\mathrm{T}}$.
- Function $\mathrm{sign}^k(\cdot)$: $\mathrm{sign}^k(q) = (\mathrm{sgn}(q_0)|q_0|^k, \mathrm{sgn}^k(\vec{q}))$ and $\mathrm{sign}^k(\boldsymbol{q}) = \mathrm{sign}^k(q_r) + \epsilon \mathrm{sign}^k(q_d)$, where $\mathrm{sgn}^k(\vec{q}) = (\mathrm{sgn}(q_1)|q_1|^k, \mathrm{sgn}(q_2)|q_2|^k, \mathrm{sgn}(q_3)|q_3|^k)^{\mathrm{T}}$ and $k \in \mathbb{R}$.
- Jacobian matrix of function $p = f(q)$: $\dfrac{\partial p}{\partial q} = \begin{bmatrix} \partial p_0/\partial q_0 & \partial p_0/\partial \vec{q}^{\mathrm{T}} \\ \partial \vec{p}/\partial q_0 & \partial \vec{p}/\partial \vec{q}^{\mathrm{T}} \end{bmatrix}$.
- Jacobian matrix of function $\boldsymbol{p} = \boldsymbol{f}(\boldsymbol{q})$: $\dfrac{\partial \boldsymbol{p}}{\partial \boldsymbol{q}} = \begin{bmatrix} \partial p_r/\partial q_r & \partial p_r/\partial q_d \\ \partial p_d/\partial q_r & \partial p_d/\partial q_d \end{bmatrix}$.

3. Relative Kinematics and Dynamics of Proximity Maneuver Based on Dual Quaternion

There are various relative position or attitude representations, which leads to different kinematics and dynamics equations [44]. The service spacecraft needs to simultaneously adjust its position and attitude, i.e., pose, relative to the target during the proximity maneuver to maintain its observation of the target. Therefore, it is necessary to use the relative kinematics and dynamics equations of a 6-DOF pose for control design. Since dual quaternions are characterized by a compact structure and unified form in equation derivations, this paper establishes relative kinematics and dynamics models for proximity maneuvering by using dual quaternions as pose representations.

3.1. Pose Representations Based on Unit Dual Quaternions

According to Euler's rotation theorem, for any two coordinate frames with the same origin in three-dimensional space, it is always possible to rotate one frame around a fixed axis passing through the origin by a certain angle to coincide with another. With this physical property of rotation, if the I-frame rotates around the axis $\vec{n}$ by the angle ϕ to coincide with the B-frame, then the orientation of B relative to I can be represented by the unit quaternion $q_{\mathrm{B/I}}$:

$$q_{\mathrm{B/I}} = (\cos(\phi/2), \sin(\phi/2) \cdot \vec{n}) \tag{4}$$

With the orientation representation $q_{\mathrm{B/I}}$ and quaternion multiplication, the calculation relationships of the coordinates for the same vector in the B-frame, $\vec{v}^{\mathrm{B}}$, and in the I-frame, $\vec{v}^{\mathrm{I}}$, are as follows:

$$\begin{cases} v^{\mathrm{B}} = q_{\mathrm{B/I}}^* v^{\mathrm{I}} q_{\mathrm{B/I}} \\ v^{\mathrm{I}} = q_{\mathrm{B/I}} v^{\mathrm{B}} q_{\mathrm{B/I}}^* \end{cases} \tag{5}$$

where $v^{\mathrm{B}} = (0, \vec{v}^{\mathrm{B}})$ and $v^{\mathrm{I}} = (0, \vec{v}^{\mathrm{I}})$ are quaternions generated by corresponding vectors.

The relative pose representation between two frames is further investigated when their origins do not coincide. If the I-frame's origin does not coincide with the B-frame's, the I-frame can be translated along the vector $\vec{r}_{\mathrm{B/I}}$, which is from the I-frame's origin to the B-frame's, until their origins coincide, and then rotated around the axis $\vec{n}$ by the angle ϕ to coincide with the B-frame. In this way, the pose of B with respect to I can be represented compactly by the unit dual quaternion $\boldsymbol{q}_{\mathrm{B/I}}$:

$$\boldsymbol{q}_{\mathrm{B/I}} = q_{\mathrm{B/I},r} + \epsilon q_{\mathrm{B/I},d} = q_{\mathrm{B/I}} + \epsilon r^{\mathrm{I}}_{\mathrm{B/I}} q_{\mathrm{B/I}}/2 = q_{\mathrm{B/I}} + \epsilon q_{\mathrm{B/I}} r^{\mathrm{B}}_{\mathrm{B/I}}/2 \tag{6}$$

where $q_{\mathrm{B/I},r}$ and $q_{\mathrm{B/I},d}$ are the real part and dual part of $\boldsymbol{q}_{\mathrm{B/I}}$, respectively, and $r^{\mathrm{I}}_{\mathrm{B/I}} = (0, \vec{r}^{\mathrm{I}}_{\mathrm{B/I}})$ and $r^{\mathrm{B}}_{\mathrm{B/I}} = (0, \vec{r}^{\mathrm{B}}_{\mathrm{B/I}})$ are quaternions generated by $\vec{r}^{\mathrm{I}}_{\mathrm{B/I}}$ and $\vec{r}^{\mathrm{B}}_{\mathrm{B/I}}$, which are coordinates of vector $\vec{r}_{\mathrm{B/I}}$ in the I-frame and B-frame, respectively. Although the coordinates of vector $\vec{r}_{\mathrm{B/I}}$ are dependent on the specific frame, the dual part $q_{\mathrm{B/I},d}$ is independent of the frame. Therefore, it does not emphasize in which frame $q_{\mathrm{B/I},d}$ is expressed. According to Equation (6), if the dual quaternion representation of the relative pose is known, $\boldsymbol{q}_{\mathrm{B/I}}$, then the relative attitude quaternion $q_{\mathrm{B/I}} = q_{\mathrm{B/I},r}$, and the relative position vector coordinates of the two frames' origins can be calculated inversely as follows:

$$\begin{cases} r^{\mathrm{I}}_{\mathrm{B/I}} = 2 q_{\mathrm{B/I},d} q^{*}_{\mathrm{B/I},r} \\ r^{\mathrm{B}}_{\mathrm{B/I}} = 2 q^{*}_{\mathrm{B/I},r} q_{\mathrm{B/I},d} \end{cases} \tag{7}$$

Similar to unit quaternions, unit dual quaternions can also transform coordinates in different frames through multiplication. For vectors $\vec{v}_r$ and $\vec{v}_d$, their coordinates $\vec{v}^{\mathrm{I}}_r$ and $\vec{v}^{\mathrm{I}}_d$ in the I-frame are combined to generate the dual quaternion $\boldsymbol{v}^{\mathrm{I}} = v^{\mathrm{I}}_r + \epsilon v^{\mathrm{I}}_d$, where $v^{\mathrm{I}}_r = (0, \vec{v}^{\mathrm{I}}_r)$ and $v^{\mathrm{I}}_d = (0, \vec{v}^{\mathrm{I}}_d)$. In the same way, their coordinates $\vec{v}^{\mathrm{B}}_r$ and $\vec{v}^{\mathrm{B}}_d$ in the B-frame generate $\boldsymbol{v}^{\mathrm{B}} = v^{\mathrm{B}}_r + \epsilon v^{\mathrm{B}}_d$, where $v^{\mathrm{B}}_r = (0, \vec{v}^{\mathrm{B}}_r)$ and $v^{\mathrm{B}}_d = (0, \vec{v}^{\mathrm{B}}_d)$. Then the relationship between $\boldsymbol{v}^{\mathrm{I}}$ and $\boldsymbol{v}^{\mathrm{B}}$ satisfies:

$$\begin{cases} \boldsymbol{q}^{*}_{\mathrm{B/I}} \boldsymbol{v}^{\mathrm{I}} \boldsymbol{q}_{\mathrm{B/I}} = v^{\mathrm{B}}_r + \epsilon (v^{\mathrm{B}}_d + v^{\mathrm{B}}_r \times r^{\mathrm{B}}_{\mathrm{B/I}}) \\ \boldsymbol{q}_{\mathrm{B/I}} \boldsymbol{v}^{\mathrm{B}} \boldsymbol{q}^{*}_{\mathrm{B/I}} = v^{\mathrm{I}}_r + \epsilon (v^{\mathrm{I}}_d - v^{\mathrm{I}}_r \times r^{\mathrm{I}}_{\mathrm{B/I}}) \end{cases} \tag{8}$$

where $v^{\mathrm{B}}_r = q^{*}_{\mathrm{B/I}} v^{\mathrm{I}}_r q_{\mathrm{B/I}}$ and $v^{\mathrm{B}}_d = q^{*}_{\mathrm{B/I}} v^{\mathrm{I}}_d q_{\mathrm{B/I}}$. Note that an extra cross product term appears in the dual part of the transformed dual quaternion in Equation (8), which stems from the unique structure and operation rules of dual quaternions.

3.2. Coordinate Frame Definition

For the determination of relative kinematics and dynamics, this paper prescribes four coordinate frames related to proximity maneuver control, as shown in Figure 1.

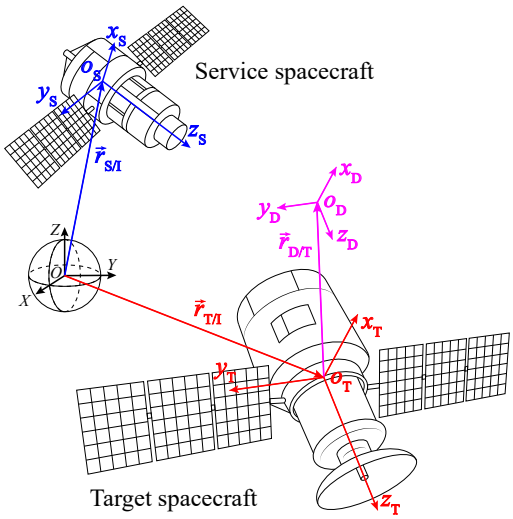

Figure 1. Diagram of coordinate frames.

(1) Earth-centered inertial frame $O - XYZ$

The origin O is at the center of mass of the Earth. The OX axis points towards the vernal equinox in the equatorial plane. The OZ axis is perpendicular to the equatorial plane and points towards the celestial north pole. The OY axis completes the right-handed orthogonal frame. This frame is used to describe the translation and rotation of spacecraft relative to inertial space.

(2) Service spacecraft body frame $o_S - x_S y_S z_S$

The origin o_S is at the center of mass of the service spacecraft. The three axes correspond to the three principal axes of inertia of the spacecraft and point outward from the spacecraft body. This frame is used to describe the body rotation of the service spacecraft relative to others, as well as the pose variations of the target observed from the service spacecraft.

(3) Target spacecraft body frame $o_T - x_T y_T z_T$

The origin o_T is at the center of mass of the target spacecraft. The three axes are along the three principal axes of inertia of the target. This frame is used to describe the body rotation of the target spacecraft relative to others, and set the desired relative pose for proximity maneuvering.

(4) Desired frame $o_D - x_D y_D z_D$

The desired frame depends on the specific mission requirements. In this paper, the origin o_D deviates from the target spacecraft by a certain position, and the orientations of three frame axes remain unchanged relative to the target. This frame is used to set control objectives. Relative hovering of the target is accomplished when the service spacecraft superimposes $o_S - x_S y_S z_S$ onto $o_D - x_D y_D z_D$ via a proximity maneuver.

3.3. Kinematics Equations of Proximity Maneuver

According to the descriptions in Section 3.1, the unit quaternion $q_{S/I}$ is used to represent the attitude orientation of $o_S - x_S y_S z_S$ relative to $O - XYZ$, i.e., the attitude orientation of the service spacecraft in inertial space. The attitude kinematics equations can be obtained by taking the time derivative of $q_{S/I}$ as follows:

$$\dot{q}_{S/I} = \omega^I_{S/I} q_{S/I}/2 = q_{S/I}\omega^S_{S/I}/2 \tag{9}$$

where $\omega^I_{S/I} = (0, \vec{\omega}^I_{S/I})$ and $\omega^S_{S/I} = (0, \vec{\omega}^S_{S/I})$. $\vec{\omega}^I_{S/I}$ and $\vec{\omega}^S_{S/I}$ are representations of the angular velocity vector $\vec{\omega}_{S/I}$ in $O - XYZ$ and $o_S - x_S y_S z_S$, respectively.

Then, the pose kinematics equations are derived on the attitude kinematics. The unit dual quaternion $\boldsymbol{q}_{S/I}$ is used to represent the pose of $o_S - x_S y_S z_S$ relative to $O - XYZ$, i.e., the pose of the service spacecraft in inertial space. According to Section 3.1, $\boldsymbol{q}_{S/I} = q_{S/I} + \epsilon r^I_{S/I} q_{S/I}/2$, taking the time derivative of $\boldsymbol{q}_{S/I}$ as follows:

$$\begin{aligned}
\dot{\boldsymbol{q}}_{S/I} &= \dot{q}_{S/I} + \epsilon(\dot{r}^I_{S/I} q_{S/I} + r^I_{S/I}\dot{q}_{S/I})/2 \\
&= \omega^I_{S/I} q_{S/I}/2 + \epsilon(\dot{r}^I_{S/I} q_{S/I} + r^I_{S/I}\omega^I_{S/I} q_{S/I}/2)/2 \\
&= \omega^I_{S/I} q_{S/I}/2 + \epsilon(\dot{r}^I_{S/I} + r^I_{S/I} \times \omega^I_{S/I} + \omega^I_{S/I} r^I_{S/I}/2) q_{S/I}/2 \\
&= (\omega^I_{S/I} + \epsilon(\dot{r}^I_{S/I} + r^I_{S/I} \times \omega^I_{S/I}))(q_{S/I} + \epsilon r^I_{S/I} q_{S/I}/2)/2
\end{aligned} \tag{10}$$

where $r^I_{S/I} = (0, \vec{r}^I_{S/I})$, $\vec{r}^I_{S/I}$ is the coordinate of $\vec{r}_{S/I}$ in $O - XYZ$, and $\dot{r}^I_{S/I}$ is the time derivative of $r^I_{S/I}$. Let $\boldsymbol{\omega}^I_{S/I} = \omega^I_{S/I} + \epsilon(\dot{r}^I_{S/I} + r^I_{S/I} \times \omega^I_{S/I})$, which is referred to as dual velocity of $o_S - x_S y_S z_S$ relative to $O - XYZ$. With the transformation Equation (8), the 6-DOF pose-coupled kinematics equations of the service spacecraft in inertial space can be derived:

$$\dot{\boldsymbol{q}}_{S/I} = \boldsymbol{\omega}^I_{S/I} \boldsymbol{q}_{S/I}/2 = \boldsymbol{q}_{S/I}\boldsymbol{\omega}^S_{S/I}/2 \tag{11}$$

where $\boldsymbol{\omega}^{S}_{S/I} = \omega^{S}_{S/I} + \epsilon \dot{r}^{S}_{S/I}$, and $\omega^{S}_{S/I} = q^{*}_{S/I}\omega^{I}_{S/I}q_{S/I}$ and $\dot{r}^{S}_{S/I} = q^{*}_{S/I}\dot{r}^{I}_{S/I}q_{S/I}$.

From the derivations of Equation (10), the real part of the dual velocity $\boldsymbol{\omega}^{I}_{S/I}$ is the quaternion generated by the attitude angular velocity vector expressed in $O - XYZ$, and the dual part is the quaternion generated by the time derivative of $\vec{r}^{S}_{S/I}$ expressed in $O - XYZ$. According to the expression of dual velocity $\boldsymbol{\omega}^{S}_{S/I}$, its real part is the quaternion generated by the attitude angular velocity vector expressed in $o_S - x_S y_S z_S$, and its dual part is the quaternion generated by the time derivative of $\vec{r}^{I}_{S/I}$ expressed in $o_S - x_S y_S z_S$.

Similarly, for the target spacecraft, the unit dual quaternion $\boldsymbol{q}_{T/I} = q_{T/I} + \epsilon r^{I}_{T/I} q_{T/I}/2$ is used to represent its pose relative to $O - XYZ$, and the time derivative of $\boldsymbol{q}_{T/I}$ is obtained as follows:

$$\dot{\boldsymbol{q}}_{T/I} = \boldsymbol{\omega}^{I}_{T/I}\boldsymbol{q}_{T/I}/2 = \boldsymbol{q}_{T/I}\boldsymbol{\omega}^{T}_{T/I}/2 \tag{12}$$

Let $\boldsymbol{q}_{S/T} = \boldsymbol{q}^{*}_{T/I}\boldsymbol{q}_{S/I}$; the calculation of $\boldsymbol{q}_{S/T}$ is as follows:

$$\begin{aligned}
\boldsymbol{q}_{S/T} &= (q_{T/I} + \epsilon r^{I}_{T/I} q_{T/I}/2)^{*}(q_{S/I} + \epsilon r^{I}_{S/I} q_{S/I}/2) \\
&= q^{*}_{T/I}q_{S/I} + \epsilon(q^{*}_{T/I}(r^{I}_{T/I})^{*}q_{S/I} + q^{*}_{T/I}r^{I}_{S/I}q_{S/I})/2 \\
&= q^{*}_{T/I}q_{S/I} + \epsilon q^{*}_{T/I}(r^{I}_{S/I} - r^{I}_{T/I})q_{S/I}/2 \\
&= q^{*}_{T/I}q_{S/I} + \epsilon q^{*}_{T/I}r^{I}_{S/T}q_{S/I}/2 \\
&= q_{S/T} + \epsilon q_{S/T}r^{S}_{S/T}/2 \\
&= q_{S/T} + \epsilon r^{T}_{S/T}q_{S/T}/2
\end{aligned} \tag{13}$$

where $q_{S/T} = q^{*}_{T/I}q_{S/I}$ is the quaternion representation of the attitude of the service spacecraft relative to the target, $r^{S}_{S/T} = (0, \vec{r}^{S}_{S/T})$, and $r^{T}_{S/T} = (0, \vec{r}^{T}_{S/T})$. $\vec{r}^{S}_{S/T}$ and $\vec{r}^{T}_{S/T}$ are coordinates of the relative position vector $\vec{r}_{S/T}$ in $o_S - x_S y_S z_S$ and $o_T - x_T y_T z_T$, respectively. It can be concluded from Equation (13) that $\boldsymbol{q}_{S/T}$ is exactly the desired dual quaternion to represent the pose of the service spacecraft relative to the target, taking the time derivative of $\boldsymbol{q}_{S/T}$ as follows:

$$\begin{aligned}
\dot{\boldsymbol{q}}_{S/T} &= \dot{\boldsymbol{q}}^{*}_{T/I}\boldsymbol{q}_{S/I} + \boldsymbol{q}^{*}_{T/I}\dot{\boldsymbol{q}}_{S/I} \\
&= -\boldsymbol{q}^{*}_{T/I}\dot{\boldsymbol{q}}_{T/I}\boldsymbol{q}^{*}_{T/I}\boldsymbol{q}_{S/I} + \boldsymbol{q}^{*}_{T/I}\boldsymbol{\omega}^{I}_{S/I}\boldsymbol{q}_{S/I}/2 \\
&= -\boldsymbol{q}^{*}_{T/I}\boldsymbol{\omega}^{I}_{T/I}\boldsymbol{q}_{T/I}\boldsymbol{q}^{*}_{T/I}\boldsymbol{q}_{S/I}/2 + \boldsymbol{q}^{*}_{T/I}\boldsymbol{\omega}^{I}_{S/I}\boldsymbol{q}_{S/I}/2 \\
&= \boldsymbol{q}^{*}_{T/I}(\boldsymbol{\omega}^{I}_{S/I} - \boldsymbol{\omega}^{I}_{T/I})\boldsymbol{q}_{S/I}/2 \\
&= \boldsymbol{q}^{*}_{T/I}\boldsymbol{q}_{S/I}(\boldsymbol{\omega}^{S}_{S/I} - \boldsymbol{\omega}^{S}_{T/I})/2
\end{aligned} \tag{14}$$

Let $\boldsymbol{\omega}^{S}_{S/T} = \boldsymbol{\omega}^{S}_{S/I} - \boldsymbol{\omega}^{S}_{T/I}$, which is referred to as the dual velocity of the service spacecraft relative to the target. Then, the 6-DOF kinematics equation of the service spacecraft relative to the target represented by the dual quaternion can be obtained:

$$\dot{\boldsymbol{q}}_{S/T} = \boldsymbol{q}_{S/T}\boldsymbol{\omega}^{S}_{S/T}/2 = \boldsymbol{\omega}^{T}_{S/T}\boldsymbol{q}_{S/T}/2 \tag{15}$$

3.4. Dynamics Equations of Proximity Maneuver

This section derives the relative dynamics equations based on the kinematics equations. With the mass and moment of inertia (calculated in $o_S - x_S y_S z_S$) of the service spacecraft denoted by m and M, respectively, the dual inertia matrix is generated as follows:

$$\mathrm{J} = \begin{bmatrix} \mathrm{J_m} & 0_{4\times4} \\ 0_{4\times4} & \mathrm{J_M} \end{bmatrix} \tag{16}$$

where $\mathrm{J_m} = \begin{bmatrix} 1 & 0_{1\times3} \\ 0_{3\times1} & \mathrm{m}\cdot\mathrm{I}_{3\times3} \end{bmatrix}$, $\mathrm{J_M} = \begin{bmatrix} 1 & 0_{1\times3} \\ 0_{3\times1} & \mathrm{M} \end{bmatrix}$, $0_{4\times4}$ is a square 4×4 zero-element matrix, $0_{3\times1}$ and $0_{1\times3}$ are zero-element vectors, and $\mathrm{I}_{3\times3}$ is a square 3×3 identity matrix. J is a symmetric positive-definite matrix according to the properties of the moment of inertia.

Let $\mathrm{J_E} = \mathrm{J}\cdot\mathrm{E}$, where $\mathrm{E} = \begin{bmatrix} 0_{4\times4} & \mathrm{I}_{4\times4} \\ \mathrm{I}_{4\times4} & 0_{4\times4} \end{bmatrix}$ is a symmetric matrix and $\mathrm{I}_{4\times4}$ is a square 4×4 identity matrix; one can further calculate $\mathrm{J_E} \circledast \boldsymbol{\omega}^{\mathrm{S}}_{\mathrm{S/I}} = (\mathrm{J_m} * \dot{r}^{\mathrm{S}}_{\mathrm{S/I}}) + \epsilon(\mathrm{J_M} * \omega^{\mathrm{S}}_{\mathrm{S/I}})$ by calculating $\boldsymbol{\omega}^{\mathrm{S}}_{\mathrm{S/I}} = \omega^{\mathrm{S}}_{\mathrm{S/I}} + \epsilon\dot{r}^{\mathrm{S}}_{\mathrm{S/I}}$, where $\circledast$ and $*$ denote the multiplication of a matrix with a dual quaternion and quaternion, respectively. Taking $o_{\mathrm{S}} - x_{\mathrm{S}}y_{\mathrm{S}}z_{\mathrm{S}}$ as the coordinate frame for calculations, it can be determined by the theorem of momentum and the theorem of moment of momentum that:

$$\begin{aligned} \frac{\mathrm{d}(\mathrm{J_E} \circledast \boldsymbol{\omega}^{\mathrm{S}}_{\mathrm{S/I}})}{\mathrm{d}t} &= ((\mathrm{J_m} * \dot{r}^{\mathrm{S}}_{\mathrm{S/I}}) + \omega^{\mathrm{S}}_{\mathrm{S/I}} \times (\mathrm{J_m} * \dot{r}^{\mathrm{S}}_{\mathrm{S/I}})) + \epsilon((\mathrm{J_M} * \dot{\omega}^{\mathrm{S}}_{\mathrm{S/I}}) + \omega^{\mathrm{S}}_{\mathrm{S/I}} \times (\mathrm{J_M} * \omega^{\mathrm{S}}_{\mathrm{S/I}})) \\ &= (\mathrm{J_m} * \dot{r}^{\mathrm{S}}_{\mathrm{S/I}}) + \epsilon(\mathrm{J_M} * \dot{\omega}^{\mathrm{S}}_{\mathrm{S/I}}) + (\omega^{\mathrm{S}}_{\mathrm{S/I}} \times (\mathrm{J_m} * \dot{r}^{\mathrm{S}}_{\mathrm{S/I}})) + \epsilon(\omega^{\mathrm{S}}_{\mathrm{S/I}} \times (\mathrm{J_M} * \omega^{\mathrm{S}}_{\mathrm{S/I}})) \\ &= \mathrm{J_E} \circledast \dot{\boldsymbol{\omega}}^{\mathrm{S}}_{\mathrm{S/I}} + \boldsymbol{\omega}^{\mathrm{S}}_{\mathrm{S/I}} \times (\mathrm{J_E} \circledast \boldsymbol{\omega}^{\mathrm{S}}_{\mathrm{S/I}}) \\ &= \boldsymbol{f}^{\mathrm{S}}_{\mathrm{G}} + \boldsymbol{f}^{\mathrm{S}}_{\mathrm{D}} + \boldsymbol{f}^{\mathrm{S}}_{\mathrm{C}} \end{aligned} \tag{17}$$

where $\boldsymbol{f}^{\mathrm{S}}_{\mathrm{G}}$, $\boldsymbol{f}^{\mathrm{S}}_{\mathrm{D}}$, and $\boldsymbol{f}^{\mathrm{S}}_{\mathrm{C}}$ are the dual quaternions formulated by the gravity and gravity gradient torque of the Earth, unmodeled disturbance force and torque, and control force and torque, respectively. The unmodeled part $\boldsymbol{f}^{\mathrm{S}}_{\mathrm{D}}$ is detailed in Section 7. The calculation of $\boldsymbol{f}^{\mathrm{S}}_{\mathrm{G}}$ is as follows:

$$\boldsymbol{f}^{\mathrm{S}}_{\mathrm{G}} = -\mu\mathrm{J_m} * r^{\mathrm{S}}_{\mathrm{S/I}} / \|\vec{r}^{\mathrm{S}}_{\mathrm{S/I}}\|^3 + \epsilon(3\mu r^{\mathrm{S}}_{\mathrm{S/I}} \times (\mathrm{J_M} * r^{\mathrm{S}}_{\mathrm{S/I}}) / \|\vec{r}^{\mathrm{S}}_{\mathrm{S/I}}\|^5) \tag{18}$$

where μ is the gravitational constant of the Earth.

The time derivative of $\boldsymbol{\omega}^{\mathrm{S}}_{\mathrm{S/T}} = \boldsymbol{\omega}^{\mathrm{S}}_{\mathrm{S/I}} - \boldsymbol{\omega}^{\mathrm{S}}_{\mathrm{T/I}}$ is calculated through kinematics relationships as follows:

$$\begin{aligned} \dot{\boldsymbol{\omega}}^{\mathrm{S}}_{\mathrm{S/T}} &= \dot{\boldsymbol{\omega}}^{\mathrm{S}}_{\mathrm{S/I}} - \dot{\boldsymbol{\omega}}^{\mathrm{S}}_{\mathrm{T/I}} \\ &= \dot{\boldsymbol{\omega}}^{\mathrm{S}}_{\mathrm{S/I}} - \mathrm{d}(\boldsymbol{q}^{*}_{\mathrm{S/T}}\boldsymbol{\omega}^{\mathrm{T}}_{\mathrm{T/I}}\boldsymbol{q}_{\mathrm{S/T}})/\mathrm{d}t \\ &= \dot{\boldsymbol{\omega}}^{\mathrm{S}}_{\mathrm{S/I}} + \boldsymbol{q}^{*}_{\mathrm{S/T}}\dot{\boldsymbol{q}}_{\mathrm{S/T}}\boldsymbol{q}^{*}_{\mathrm{S/T}}\boldsymbol{\omega}^{\mathrm{T}}_{\mathrm{T/I}}\boldsymbol{q}_{\mathrm{S/T}} - \boldsymbol{q}^{*}_{\mathrm{S/T}}\dot{\boldsymbol{\omega}}^{\mathrm{T}}_{\mathrm{T/I}}\boldsymbol{q}_{\mathrm{S/T}} - \boldsymbol{q}^{*}_{\mathrm{S/T}}\boldsymbol{\omega}^{\mathrm{T}}_{\mathrm{T/I}}\dot{\boldsymbol{q}}_{\mathrm{S/T}} \\ &= \dot{\boldsymbol{\omega}}^{\mathrm{S}}_{\mathrm{S/I}} - \boldsymbol{q}^{*}_{\mathrm{S/T}}\dot{\boldsymbol{\omega}}^{\mathrm{T}}_{\mathrm{T/I}}\boldsymbol{q}_{\mathrm{S/T}} + \boldsymbol{\omega}^{\mathrm{S}}_{\mathrm{S/T}}\boldsymbol{\omega}^{\mathrm{S}}_{\mathrm{T/I}}/2 - \boldsymbol{\omega}^{\mathrm{S}}_{\mathrm{T/I}}\boldsymbol{\omega}^{\mathrm{S}}_{\mathrm{S/T}}/2 \\ &= \dot{\boldsymbol{\omega}}^{\mathrm{S}}_{\mathrm{S/I}} - \boldsymbol{q}^{*}_{\mathrm{S/T}}\dot{\boldsymbol{\omega}}^{\mathrm{T}}_{\mathrm{T/I}}\boldsymbol{q}_{\mathrm{S/T}} + \boldsymbol{\omega}^{\mathrm{S}}_{\mathrm{S/T}} \times \boldsymbol{\omega}^{\mathrm{S}}_{\mathrm{T/I}} + \boldsymbol{\omega}^{\mathrm{S}}_{\mathrm{S/T}} \times \boldsymbol{\omega}^{\mathrm{S}}_{\mathrm{S/T}} \\ &= \dot{\boldsymbol{\omega}}^{\mathrm{S}}_{\mathrm{S/I}} - \boldsymbol{q}^{*}_{\mathrm{S/T}}\dot{\boldsymbol{\omega}}^{\mathrm{T}}_{\mathrm{T/I}}\boldsymbol{q}_{\mathrm{S/T}} + \boldsymbol{\omega}^{\mathrm{S}}_{\mathrm{S/T}} \times \boldsymbol{\omega}^{\mathrm{S}}_{\mathrm{S/I}} \end{aligned} \tag{19}$$

Combining Equations (17) and (19), the 6-DOF dynamics equation of the service spacecraft relative to the target spacecraft represented by the dual quaternion can be obtained:

$$\dot{\boldsymbol{\omega}}^{\mathrm{S}}_{\mathrm{S/T}} = \mathrm{J}^{-1}_{\mathrm{E}} \circledast (\boldsymbol{f}^{\mathrm{S}}_{\mathrm{G}} + \boldsymbol{f}^{\mathrm{S}}_{\mathrm{D}} + \boldsymbol{f}^{\mathrm{S}}_{\mathrm{C}} - \boldsymbol{\omega}^{\mathrm{S}}_{\mathrm{S/I}} \times (\mathrm{J_E} \circledast \boldsymbol{\omega}^{\mathrm{S}}_{\mathrm{S/I}})) - \boldsymbol{q}^{*}_{\mathrm{S/T}}\dot{\boldsymbol{\omega}}^{\mathrm{T}}_{\mathrm{T/I}}\boldsymbol{q}_{\mathrm{S/T}} + \boldsymbol{\omega}^{\mathrm{S}}_{\mathrm{S/T}} \times \boldsymbol{\omega}^{\mathrm{S}}_{\mathrm{S/I}} \tag{20}$$

3.5. Unknown Integrated Disturbances

It is impossible to accurately calculate $\boldsymbol{f}^{\mathrm{S}}_{\mathrm{D}}$ because it is related to various unknown disturbance forces and torques, which may decrease the control performance of the proximity maneuver. This is a negligible problem when two spacecraft are far apart. However, maneuver error may cause spacecraft collision or the target intermittently being out of the observation field of view when they are in close range. Sliding-mode control can effectively cope with uncertain disturbances, but easily leads to chattering in control. In addition, it is very difficult to obtain $\dot{\boldsymbol{\omega}}^{\mathrm{T}}_{\mathrm{T/I}}$, i.e., the translation and rotation acceleration of noncooperative target spacecraft, which further increases unknown uncertainty. In order to deal with the negative effects of the aforementioned two types of uncertainties on proximity maneuver control, unknown space disturbances and maneuver acceleration of the target are formulated as unknown integrated disturbances $\boldsymbol{d}^{\mathrm{S}}$. Then, Equation (20) is rewritten as follows:

$$\dot{\boldsymbol{\omega}}^{\mathrm{S}}_{\mathrm{S/T}} = \mathrm{J}^{-1}_{\mathrm{E}} \circledast (\boldsymbol{f}^{\mathrm{S}}_{\mathrm{G}} + \boldsymbol{f}^{\mathrm{S}}_{\mathrm{C}} - \boldsymbol{\omega}^{\mathrm{S}}_{\mathrm{S/I}} \times (\mathrm{J_E} \circledast \boldsymbol{\omega}^{\mathrm{S}}_{\mathrm{S/I}})) + \boldsymbol{\omega}^{\mathrm{S}}_{\mathrm{S/T}} \times \boldsymbol{\omega}^{\mathrm{S}}_{\mathrm{S/I}} + \boldsymbol{d}^{\mathrm{S}} \tag{21}$$

where $\boldsymbol{d}^{\mathrm{S}} = \mathrm{J}_{\mathrm{E}}^{-1} \circledast \boldsymbol{f}_{\mathrm{D}}^{\mathrm{S}} - \boldsymbol{q}_{\mathrm{S/T}}^{*} \dot{\boldsymbol{\omega}}_{\mathrm{T/I}}^{\mathrm{T}} \boldsymbol{q}_{\mathrm{S/T}}$ is an unknown term, calculated in the body frame $o_{\mathrm{S}} - x_{\mathrm{S}} y_{\mathrm{S}} z_{\mathrm{S}}$.

In the subsequent ESO design, the $\boldsymbol{d}^{\mathrm{S}}$ will be treated as the state variable. If we enote the time derivative of $\boldsymbol{d}^{\mathrm{S}}$ as $\boldsymbol{\alpha}$, we can obtain an extended state equation:

$$\dot{\boldsymbol{d}}^{\mathrm{S}} = \boldsymbol{\alpha} \tag{22}$$

4. Design of ESO

Inspired by the STA [45,46], this paper designs an ESO to estimate unknown integrated disturbances. The estimated disturbances will be incorporated into the control law to ensure the tracking accuracy of the noncooperative target during proximity maneuvering. The ESO corresponding to Equations (21) and (22) is as follows:

$$\begin{cases} \dot{\hat{\boldsymbol{\omega}}}_{\mathrm{S/T}}^{\mathrm{S}} = \mathrm{J}_{\mathrm{E}}^{-1} \circledast (\boldsymbol{f}_{\mathrm{G}}^{\mathrm{S}} + \boldsymbol{f}_{\mathrm{C}}^{\mathrm{S}} - \boldsymbol{\omega}_{\mathrm{S/I}}^{\mathrm{S}} \times (\mathrm{J}_{\mathrm{E}} \circledast \boldsymbol{\omega}_{\mathrm{S/I}}^{\mathrm{S}})) + \boldsymbol{\omega}_{\mathrm{S/T}}^{\mathrm{S}} \times \boldsymbol{\omega}_{\mathrm{S/I}}^{\mathrm{S}} + \hat{\boldsymbol{d}}^{\mathrm{S}} + \mathrm{K}_1 \circledast \boldsymbol{\Theta}(\Delta\boldsymbol{\omega}/\delta) \\ \dot{\hat{\boldsymbol{d}}}^{\mathrm{S}} = \mathrm{K}_2 \circledast \boldsymbol{\Phi}(\Delta\boldsymbol{\omega}/\delta)/\delta \end{cases} \tag{23}$$

where $\hat{\boldsymbol{\omega}}_{\mathrm{S/T}}^{\mathrm{S}}$ and $\hat{\boldsymbol{d}}^{\mathrm{S}}$ are estimated values of $\boldsymbol{\omega}_{\mathrm{S/T}}^{\mathrm{S}}$ and $\boldsymbol{d}^{\mathrm{S}}$, respectively, $\Delta\boldsymbol{\omega} = \boldsymbol{\omega}_{\mathrm{S/T}}^{\mathrm{S}} - \hat{\boldsymbol{\omega}}_{\mathrm{S/T}}^{\mathrm{S}}$ is the estimated error, $\delta > 0$ is a gain constant, and both $\mathrm{K}_1 = \mathrm{diag}(\mathrm{k}_{11}, \cdots, \mathrm{k}_{18})$ and $\mathrm{K}_2 = \mathrm{diag}(\mathrm{k}_{21}, \cdots, \mathrm{k}_{28})$ are positive-definite diagonal matrices. In ESO (23), $\boldsymbol{\omega}_{\mathrm{S/T}}^{\mathrm{S}}$ and $\boldsymbol{\omega}_{\mathrm{S/I}}^{\mathrm{S}}$ are treated as the values of the measured states, and $\boldsymbol{f}_{\mathrm{G}}^{\mathrm{S}}$ and $\boldsymbol{f}_{\mathrm{C}}^{\mathrm{S}}$ can be calculated using the measured states. The functions $\boldsymbol{\Theta}(\boldsymbol{x})$ and $\boldsymbol{\Phi}(\boldsymbol{x})$ of $\boldsymbol{x}$ are as follows:

$$\begin{cases} \boldsymbol{\Theta}(\boldsymbol{x}) = \kappa_1 \mathrm{sign}^{1/2}(\boldsymbol{x}) + \kappa_2 \boldsymbol{x} \\ \boldsymbol{\Phi}(\boldsymbol{x}) = 0.5\kappa_1^2 \mathrm{sign}(\boldsymbol{x}) + 1.5\kappa_1\kappa_2 \mathrm{sign}^{1/2}(\boldsymbol{x}) + \kappa_2^2 \boldsymbol{x} \end{cases} \tag{24}$$

where both $\kappa_1 > 0$ and $\kappa_2 > 0$ are constants.

Proposition 1. *If the time derivatives of unknown integrated disturbances satisfy* $\sqrt{\boldsymbol{\alpha} \circ \boldsymbol{\alpha}} \leqslant \mathrm{C}$, *where* C *is a constant, then the estimated errors of ESO* (23) *for the dual velocity* $\boldsymbol{\omega}_{\mathrm{S/T}}^{\mathrm{S}}$ *and the integrated disturbances* $\boldsymbol{d}^{\mathrm{S}}$ *are able to converge to* $\mathbf{0}$ *in a finite time. And the upper bound of the convergence time,* $T_{\max}$, *is estimated as follows:*

$$T_{\max} = \frac{\delta}{\chi \kappa_2} \ln(V_{1,0}^{1/2}/\vartheta + 1) \tag{25}$$

where both $\chi > 0$ *and* $\vartheta > 0$ *are constants, and* $V_{1,0} > 0$ *is related to the initial estimated errors.*

Proof of Proposition 1. Denote the estimated errors of $\boldsymbol{d}^{\mathrm{S}}$ as $\Delta\boldsymbol{d} = \boldsymbol{d}^{\mathrm{S}} - \hat{\boldsymbol{d}}^{\mathrm{S}}$. The differential equations of $\Delta\boldsymbol{\omega}$ and $\Delta\boldsymbol{d}$ are obtained by Equations (21)–(23) as follows:

$$\begin{cases} \Delta\dot{\boldsymbol{\omega}} = -\mathrm{K}_1 \circledast \boldsymbol{\Theta}(\Delta\boldsymbol{\omega}/\delta) + \Delta\boldsymbol{d} \\ \Delta\dot{\boldsymbol{d}} = -\mathrm{K}_2 \circledast \boldsymbol{\Phi}(\Delta\boldsymbol{\omega}/\delta)/\delta + \boldsymbol{\alpha} \end{cases} \tag{26}$$

Let $\boldsymbol{\eta}_1(t) = \Delta\boldsymbol{\omega}(\delta \cdot t)/\delta$ and $\boldsymbol{\eta}_2(t) = \Delta\boldsymbol{d}(\delta \cdot t)$, Equation (26) can be transformed into

$$\begin{cases} \dot{\boldsymbol{\eta}}_1 = -\mathrm{K}_1 \circledast \boldsymbol{\Theta}(\boldsymbol{\eta}_1) + \boldsymbol{\eta}_2 \\ \dot{\boldsymbol{\eta}}_2 = -\mathrm{K}_2 \circledast \boldsymbol{\Phi}(\boldsymbol{\eta}_1) + \delta \cdot \boldsymbol{\alpha}(\delta \cdot t) \end{cases} \tag{27}$$

The elements of $\boldsymbol{\eta}_1$, $\boldsymbol{\eta}_2$, $\boldsymbol{\Theta}$, $\boldsymbol{\Phi}$, and $\boldsymbol{\alpha}$ are written out, respectively, as follows:

$$\begin{cases} \boldsymbol{\eta}_1 = (\eta_{11}, (\eta_{12}, \eta_{13}, \eta_{14})^{\mathrm{T}}) + \epsilon(\eta_{15}, (\eta_{16}, \eta_{17}, \eta_{18})^{\mathrm{T}}) \\ \boldsymbol{\eta}_2 = (\eta_{21}, (\eta_{22}, \eta_{23}, \eta_{24})^{\mathrm{T}}) + \epsilon(\eta_{25}, (\eta_{26}, \eta_{27}, \eta_{28})^{\mathrm{T}}) \\ \boldsymbol{\Theta} = (\Theta_1, (\Theta_2, \Theta_3, \Theta_4)^{\mathrm{T}}) + \epsilon(\Theta_5, (\Theta_6, \Theta_7, \Theta_8)^{\mathrm{T}}) \\ \boldsymbol{\Phi} = (\Phi_1, (\Phi_2, \Phi_3, \Phi_4)^{\mathrm{T}}) + \epsilon(\Phi_5, (\Phi_6, \Phi_7, \Phi_8)^{\mathrm{T}}) \\ \boldsymbol{\alpha} = (\alpha_1, (\alpha_2, \alpha_3, \alpha_4)^{\mathrm{T}}) + \epsilon(\alpha_5, (\alpha_6, \alpha_7, \alpha_8)^{\mathrm{T}}) \end{cases} \tag{28}$$

The Jacobian matrix of the function, $\boldsymbol{\Theta} = \boldsymbol{\Theta}(\boldsymbol{\eta}_1)$, can be calculated:

$$W = \partial\boldsymbol{\Theta}(\boldsymbol{\eta}_1)/\partial\boldsymbol{\eta}_1 = \mathrm{diag}(0.5\kappa_1/|\eta_{11}|^{1/2} + \kappa_2, \cdots, 0.5\kappa_1/|\eta_{18}|^{1/2} + \kappa_2) \tag{29}$$

According to Equations (24) and (29), one can obtain:

$$\begin{cases} \dot{\boldsymbol{\Theta}} = \partial\boldsymbol{\Theta}(\boldsymbol{\eta}_1)/\partial\boldsymbol{\eta}_1 \circledast \dot{\boldsymbol{\eta}}_1 = W \circledast \dot{\boldsymbol{\eta}}_1 \\ \boldsymbol{\Phi}(\boldsymbol{\eta}_1) = W \circledast \boldsymbol{\Theta}(\boldsymbol{\eta}_1) \end{cases} \tag{30}$$

We construct the vectors $\vec{\eta} = (\Theta_1, \eta_{21}, \cdots, \Theta_8, \eta_{28})^{\mathrm{T}}$ and $\vec{\alpha} = (0, \alpha_1, \cdots, 0, \alpha_8)^{\mathrm{T}}$; then, $\dot{\vec{\eta}}$ is obtained by Equations (26)–(30):

$$\dot{\vec{\eta}} = \mathrm{diag}(\widetilde{W}_1, \cdots, \widetilde{W}_8)\mathrm{diag}(\widetilde{\mathrm{K}}_1, \cdots, \widetilde{\mathrm{K}}_8)\vec{\eta} + \delta\vec{\alpha} = \widetilde{W}\widetilde{\mathrm{K}}\vec{\eta} + \delta\vec{\alpha} \tag{31}$$

where $\widetilde{W}_i = \begin{bmatrix} w_i & 0 \\ 0 & w_i \end{bmatrix}$, $w_i = 0.5\kappa_1/|\eta_{1i}|^{1/2} + \kappa_2$, $\widetilde{\mathrm{K}}_i = \begin{bmatrix} -\mathrm{k}_{1i} & 1 \\ -\mathrm{k}_{2i} & 0 \end{bmatrix}$, $i = 1, \cdots, 8$.

Since both K_1 and K_2 are positive-definite, $\widetilde{\mathrm{K}}_i$ is a Hurwitz matrix. Then, for any symmetric positive-definite matrix Q_i, there always exist a positive-definite matrix P_i satisfying the algebraic Lyapunov equation $\widetilde{\mathrm{K}}_i^{\mathrm{T}}\mathrm{P}_i + \mathrm{P}_i\widetilde{\mathrm{K}}_i = -\mathrm{Q}_i$. The candidate Lyapunov function $V_1(\vec{\eta}\,)$ is constructed as a quadratic function of $\vec{\eta}$:

$$V_1(\vec{\eta}\,) = \sum_{i=1}^{8} \vec{\eta}_i^{\mathrm{T}}\mathrm{P}_i\vec{\eta}_i = \vec{\eta}^{\mathrm{T}}\mathrm{P}\vec{\eta} \tag{32}$$

where $\vec{\eta}_i = (\Theta_i, \eta_{2i})^{\mathrm{T}}$, and $\mathrm{P} = \mathrm{diag}(\mathrm{P}_1, \cdots, \mathrm{P}_8)$ is a symmetric positive-definite matrix. Finding out the time derivative of $V_1(\vec{\eta}\,)$ yields:

$$\begin{aligned} \dot{V}_1(\vec{\eta}\,) &= \dot{\vec{\eta}}^{\mathrm{T}}\mathrm{P}\vec{\eta} + \vec{\eta}^{\mathrm{T}}\mathrm{P}\dot{\vec{\eta}} \\ &= (\widetilde{W}\widetilde{\mathrm{K}}\vec{\eta} + \delta\vec{\alpha})^{\mathrm{T}}\mathrm{P}\vec{\eta} + \vec{\eta}^{\mathrm{T}}\mathrm{P}(\widetilde{W}\widetilde{\mathrm{K}}\vec{\eta} + \delta\vec{\alpha}) \\ &= \vec{\eta}^{\mathrm{T}}(\widetilde{\mathrm{K}}^{\mathrm{T}}\widetilde{W}^{\mathrm{T}}\mathrm{P} + \mathrm{P}\widetilde{W}\widetilde{\mathrm{K}})\vec{\eta} + 2\delta\vec{\alpha}^{\mathrm{T}}\mathrm{P}\vec{\eta} \end{aligned} \tag{33}$$

Due to the special form of $\widetilde{W}$, $\widetilde{\mathrm{K}}$, and P, $\widetilde{\mathrm{K}}^{\mathrm{T}}\widetilde{W}^{\mathrm{T}} = \widetilde{W}^{\mathrm{T}}\widetilde{\mathrm{K}}^{\mathrm{T}} = \widetilde{W}\widetilde{\mathrm{K}}^{\mathrm{T}}$ and $\mathrm{P}\widetilde{W} = \widetilde{W}\mathrm{P}$ hold, which leads to:

$$\begin{aligned} \dot{V}_1(\vec{\eta}\,) &= \vec{\eta}^{\mathrm{T}}\widetilde{W}(\widetilde{\mathrm{K}}^{\mathrm{T}}\mathrm{P} + \mathrm{P}\widetilde{\mathrm{K}})\vec{\eta} + 2\delta\vec{\alpha}^{\mathrm{T}}\mathrm{P}\vec{\eta} \\ &= -\vec{\eta}^{\mathrm{T}}\widetilde{W}\mathrm{Q}\vec{\eta} + 2\delta\vec{\alpha}^{\mathrm{T}}\mathrm{P}\vec{\eta} \\ &= -\sum_{i=1}^{8} w_i\vec{\eta}_i^{\mathrm{T}}\mathrm{Q}_i\vec{\eta}_i + 2\delta\vec{\alpha}^{\mathrm{T}}\mathrm{P}\vec{\eta} \end{aligned} \tag{34}$$

where $\mathrm{Q} = \mathrm{diag}(\mathrm{Q}_1, \cdots, \mathrm{Q}_8)$ is a symmetric positive-definite matrix.

From Equation (24), one can obtain:

$$\kappa_1|\eta_{1i}|^{1/2} \leqslant |\Theta_i| \leqslant \|\vec{\eta}_i\| \tag{35}$$

Therefore, $w_i \geqslant 0.5\kappa_1^2/\|\vec{\eta}_i\| + \kappa_2$ holds.

Using $\lambda_{\min}(\cdot)$ and $\lambda_{\max}(\cdot)$ to represent the minimum and maximum eigenvalues of the matrix, respectively, we have $\lambda_{\min}(\mathrm{P}_i)\|\vec{\eta}_i\|^2 \leqslant \vec{\eta}_i^{\mathrm{T}}\mathrm{P}_i\vec{\eta}_i \leqslant \lambda_{\max}(\mathrm{P}_i)\|\vec{\eta}_i\|^2$ and $\lambda_{\min}(\mathrm{P})\|\vec{\eta}\|^2 \leqslant \vec{\eta}^{\mathrm{T}}\mathrm{P}\vec{\eta}$, which further leads to:

$$\begin{aligned}\dot{V}_1(\vec{\eta}\,) &\leqslant -\sum_{i=1}^{8}(0.5\kappa_1^2/\|\vec{\eta}_i\|+\kappa_2)\lambda_{\min}(\mathrm{Q}_i)\|\vec{\eta}_i\|^2+2\delta\sqrt{\boldsymbol{\alpha}\circ\boldsymbol{\alpha}}\|\mathrm{P}\|\|\vec{\eta}\|\\ &\leqslant -\sum_{i=1}^{8}\lambda_{\min}(\mathrm{Q}_i)\left(\frac{\kappa_1^2(\vec{\eta}_i^{\mathrm{T}}\mathrm{P}_i\vec{\eta}_i)^{1/2}}{2\lambda_{\max}^{1/2}(\mathrm{P}_i)}+\frac{\kappa_2\vec{\eta}_i^{\mathrm{T}}\mathrm{P}_i\vec{\eta}_i}{\lambda_{\max}(\mathrm{P}_i)}\right)+\frac{2\delta\mathrm{C}\|\mathrm{P}\|}{\lambda_{\min}^{1/2}(\mathrm{P})}(\vec{\eta}^{\mathrm{T}}\mathrm{P}\vec{\eta}\,)^{1/2}\\ &\leqslant -2\gamma\kappa_1^2\sum_{i=1}^{8}(\vec{\eta}_i^{\mathrm{T}}\mathrm{P}_i\vec{\eta}_i)^{1/2}-2\chi\kappa_2\sum_{i=1}^{8}\vec{\eta}_i^{\mathrm{T}}\mathrm{P}_i\vec{\eta}_i+2\delta\sigma(\vec{\eta}^{\mathrm{T}}\mathrm{P}\vec{\eta}\,)^{1/2}\end{aligned} \tag{36}$$

where $\gamma=\min(\gamma_1,\cdots,\gamma_8)$, $\gamma_i=0.25\lambda_{\min}(\mathrm{Q}_i)/\lambda_{\max}^{1/2}(\mathrm{P}_i)$, $\chi=\min(\chi_1,\cdots,\chi_8)$, $\chi_i=0.5\lambda_{\min}(\mathrm{Q}_i)/\lambda_{\max}(\mathrm{P}_i)$, and $\sigma=\mathrm{C}\|\mathrm{P}\|/\lambda_{\min}^{1/2}(\mathrm{P})$. Combining Equations (32) and (36) yields:

$$\dot{V}_1\leqslant -2(\gamma\kappa_1^2-\delta\sigma)V_1^{1/2}-2\chi\kappa_2V_1 \tag{37}$$

Since γ, χ, σ, κ_1, and κ_2 are all positive constants, choosing $\delta\leqslant\gamma\kappa_1^2/\sigma$ inevitably leads to $\dot{V}_1\leqslant 0$ ($\dot{V}_1=0$ if and only if $V_1=0$), which indicates that $V_1(\vec{\eta}\,)$ is a strong Lyapunov function. Therefore, the trajectory of $\vec{\eta}$ will converge to the origin in a finite time.

According to Equation (37), one has:

$$V_1^{1/2}\leqslant(V_{1,0}^{1/2}+\vartheta)\mathrm{e}^{-\chi\kappa_2 t}-\vartheta \tag{38}$$

where $V_{1,0}$ is the initial value of V_1, and $\vartheta=(\gamma\kappa_1^2-\delta\sigma)/(\chi\kappa_2)>0$. The upper bound on the time that $\vec{\eta}$ converges to the origin can be further estimated as follows:

$$t_{\max}=\frac{\ln(V_{1,0}^{1/2}/\vartheta+1)}{\chi\kappa_2} \tag{39}$$

Since the elements of $\vec{\eta}$ are from recombination of the elements of $\boldsymbol{\eta}_2$ and $\boldsymbol{\Theta}$, both $\boldsymbol{\eta}_2$ and $\boldsymbol{\Theta}$ also converge to $\mathbf{0}$ in time $t_{\max}$. According to Equation (24), $\boldsymbol{\Theta}=\boldsymbol{\Theta}(\boldsymbol{\eta}_1)$ is bijective, and $\boldsymbol{\eta}_1$ also converges to $\mathbf{0}$ in time $t_{\max}$. Therefore, $\Delta\boldsymbol{\omega}(t)=\delta\cdot\boldsymbol{\eta}_1(t/\delta)$ and $\Delta\boldsymbol{d}(t)=\boldsymbol{\eta}_2(t/\delta)$ converge to $\mathbf{0}$ in time $T_{\max}=\delta\cdot t_{\max}$. □

Remark 1. *Proposition 1 is based on the hypothesis that time derivatives of unknown integrated disturbances $\boldsymbol{\alpha}$ are finite. The unknown integrated disturbances $\boldsymbol{d}^{\mathrm{S}}$ include unmodeled space disturbances $\boldsymbol{f}_{\mathrm{D}}^{\mathrm{S}}$ and maneuver accelerations of the target spacecraft $\dot{\boldsymbol{\omega}}_{\mathrm{T/I}}^{\mathrm{T}}$. They are related to the positions and velocities of service the spacecraft, and the ability of the actuators of the target. Therefore, finite $\boldsymbol{\alpha}$ represents the limited maneuver capabilities of service spacecraft and actuator performance of the target. This hypothesis is applicable in practice.*

Remark 2. *Proposition 1 indicates that the ESO (23) can effectively estimate unknown integrated disturbances. Therefore, in the design of proximity maneuver tracking control, the estimated disturbances can be used as compensation terms to suppress their negative effects.*

5. Constraint Modeling

The scenario considered in this paper is that the service spacecraft performs proximity maneuvering and visual observation around the target, and stably tracks it. There are two constraints on the relative poses of the two spacecraft during the whole process. On the one hand, the service spacecraft needs to keep the target within the observable range of the camera, resulting in an FOV constraint. On the other hand, the relative motion in proximity leads to a risk of collision for the two spacecraft, which introduces a collision avoidance constraint.

5.1. FOV Constraint Model

The construction of an FOV constraint is based on the workable observation envelope of the camera. In this paper, the camera uses a circular lens, and a cone is accordingly selected as the observation envelope. The constraints on observation are first established through geometric relationships, and then transformed into constraints on the relative pose dual quaternion $\boldsymbol{q}_{\mathrm{S/T}}$.

5.1.1. Geometric Constraints on Observation

Without loss of generality, it is assumed that the axis of the camera lens coincides with the $o_{\mathrm{S}}z_{\mathrm{S}}$ axis of the service spacecraft body frame, and the vertex of the cone envelope, N, is the intersection of the lens surface and the $o_{\mathrm{S}}z_{\mathrm{S}}$ axis, as shown in Figure 2. The position coordinates of N are $(0, 0, \mathrm{z_N})^{\mathrm{T}}$ in the $o_{\mathrm{S}} - x_{\mathrm{S}}y_{\mathrm{S}}z_{\mathrm{S}}$. In theory, the workable observation envelope of the camera is an infinitely high cone. The half FOV is denoted by θ, which depends on the performance of the camera itself.

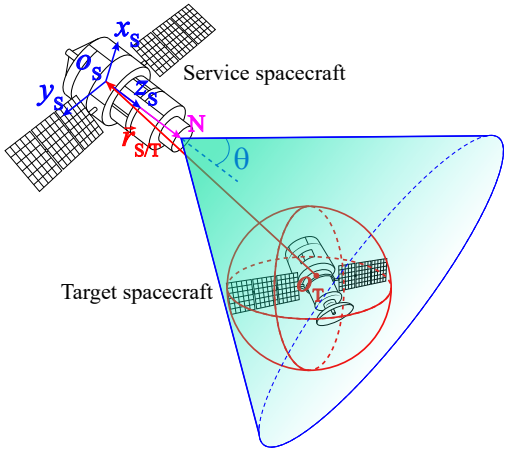

Figure 2. Conical FOV constraint.

To deal with observation constraint, current studies tend to treat the target spacecraft as a mass point, and directly confine the motion of the point within the FOV. This method may lead to incomplete observation when the target is near the FOV boundary because the camera can actually observe only a part of the target and the part outside the boundary is undetectable. To solve this problem, this paper takes the shape of the target spacecraft into account, and a sphere with a radius of $\mathrm{R_T}$ is used as its envelope. With the camera FOV and the target envelope, a new envelope is formed to constrain the position of the target centroid in the FOV of the service spacecraft. In this way, incomplete observation of the target during the proximity maneuver is effectively avoided.

To derive the new envelope equation, the FOV boundary profile on the $o_{\mathrm{S}} - x_{\mathrm{S}}z_{\mathrm{S}}$ plane is drawn as shown in Figure 3. When the target spacecraft moves within the FOV of camera, since the target envelope is a sphere, the new envelope can be obtained by translating the original FOV boundary along the $o_{\mathrm{S}}z_{\mathrm{S}}$ axis by some distance. The new vertex is denoted by N′, whose position coordinates are $(0, 0, \mathrm{z_N} + \mathrm{R_T}/\sin\theta)^{\mathrm{T}}$; then, envelope equation for the motion of o_{T} in $o_{\mathrm{S}} - x_{\mathrm{S}}y_{\mathrm{S}}z_{\mathrm{S}}$ is as follows:

$$z = (\cot\theta)\sqrt{x^2 + y^2} + \mathrm{z_{N'}} \tag{40}$$

where $\mathrm{z_{N'}} = \mathrm{z_N} + \mathrm{R_T}/\sin\theta$. If o_{T} is kept within the new envelope in the frame $o_{\mathrm{S}} - x_{\mathrm{S}}y_{\mathrm{S}}z_{\mathrm{S}}$, then vector $\vec{r}^{\,\mathrm{S}}_{\mathrm{S/T}}$ should satisfy:

$$\beta_{\mathrm{FOV}} = -\vec{\mathrm{u}}\cdot\vec{r}^{\,\mathrm{S}}_{\mathrm{S/T}} - (\cot\theta)\|\mathrm{U}\vec{r}^{\,\mathrm{S}}_{\mathrm{S/T}}\| - \mathrm{z_{N'}} > 0 \tag{41}$$

where $\vec{\mathrm{u}} = (0, 0, 1)^{\mathrm{T}}$ and $\mathrm{U} = \mathrm{diag}(1, 1, 0)$.

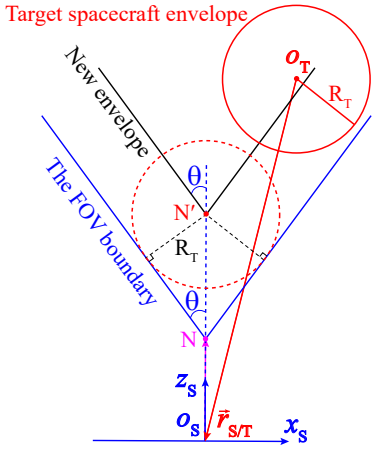

Figure 3. FOV boundary profile on $o_S - x_S z_S$ plane.

5.1.2. Dual Quaternion Representation of FOV Constraint

In Equation (41), $\beta_{FOV} = \beta_{FOV}(\vec{r}^{\,S}_{S/T})$ is the function of $\vec{r}^{\,S}_{S/T}$, and $\beta_{FOV} > 0$ is used as the constraint on the centroid position of the target spacecraft. However, this paper uses dual quaternions to represent the relative pose of the two spacecraft, and therefore, it is necessary to find out the function $\beta_{FOV} = \beta_{FOV}(\boldsymbol{q}_{S/T})$ with $\boldsymbol{q}_{S/T}$ as the independent variable. There exists the following:

$$\vec{u} \cdot \vec{r}^{\,S}_{S/T} = q_{\vec{u}} \cdot (q^*_{S/T} q_{S/T} r^S_{S/T}) = (q_{S/T} r^S_{S/T}) \cdot (q_{S/T} q_{\vec{u}}) \tag{42}$$

where $q_{\vec{u}} = (0, \vec{u})$ is a dual quaternion generated by $\vec{u}$. Then,

$$q_{S/T} q_{\vec{u}} = [q_{\vec{u}}]_\times * q_{S/T} \tag{43}$$

where $[q_{\vec{u}}]_\times = \begin{bmatrix} 0 & -\vec{u}^{\,T} \\ \vec{u} & -[\vec{u}] \end{bmatrix}$. From Equations (42) and (43), we obtain:

$$\vec{u} \cdot \vec{r}^{\,S}_{S/T} = (q_{S/T} r^S_{S/T}) \cdot ([q_{\vec{u}}]_\times * q_{S/T}) = \boldsymbol{q}_{S/T} \circ (K_{\vec{u}} \circledast \boldsymbol{q}_{S/T}) \tag{44}$$

where $K_{\vec{u}} = \begin{bmatrix} 0_{4\times4} & [q_{\vec{u}}]^T_\times \\ [q_{\vec{u}}]_\times & 0_{4\times4} \end{bmatrix} = \begin{bmatrix} 0_{4\times4} & -[q_{\vec{u}}]_\times \\ [q_{\vec{u}}]_\times & 0_{4\times4} \end{bmatrix}$ is a symmetric matrix. One further obtains:

$$\begin{aligned} \|U\vec{r}^{\,S}_{S/T}\|^2 &= \vec{r}^{\,S}_{S/T} \cdot \vec{r}^{\,S}_{S/T} - (\vec{u} \cdot \vec{r}^{\,S}_{S/T})^2 \\ &= (q_{S/T} r^S_{S/T}) \cdot (q_{S/T} r^S_{S/T}) - (\boldsymbol{q}_{S/T} \circ (K_{\vec{u}} \circledast \boldsymbol{q}_{S/T}))^2 \\ &= 4(\boldsymbol{q}_{S/T} \circ \boldsymbol{q}_{S/T} - 1) - (\boldsymbol{q}_{S/T} \circ (K_{\vec{u}} \circledast \boldsymbol{q}_{S/T}))^2 \end{aligned} \tag{45}$$

Combining Equations (41), (44) and (45) yields:

$$\beta_{FOV} = -\beta_T - (\cot\theta)\sqrt{4(\boldsymbol{q}_{S/T} \circ \boldsymbol{q}_{S/T} - 1) - \beta_T^2} - z_{N'} > 0 \tag{46}$$

where $\beta_T = \boldsymbol{q}_{S/T} \circ (K_{\vec{u}} \circledast \boldsymbol{q}_{S/T})$. Equation (46) is exactly the FOV constraint represented in terms of the dual quaternion $\boldsymbol{q}_{S/T}$.

5.2. Collision Avoidance Constraint Model

A collision may occur during the observation of target spacecraft due to the close range of the service spacecraft during a proximity maneuver. For the spacecraft's safety, collision avoidance control is necessary, which requires that the shapes of the spacecraft do not overlap in space. However, spacecraft have various shapes, some of which are complex, making it difficult to obtain their accurate shape models, especially for noncooperative targets. Furthermore, even if accurate models are established, mathematical equations of

models are very cumbersome. Therefore, simple geometries, such as spheres, ellipsoids, polyhedrons, etc., are generally used as models to conservatively describe the overall shape of spacecraft to keep them from potential superposition via active control. The envelope of a target was constructed as a sphere in FOV constraint modeling. A sphere with radius R_S was also used as the envelope of the service spacecraft in collision avoidance. The condition that the two spacecraft do not collide is as follows:

$$\beta_{CA} = \|\vec{r}^{S}_{S/T}\|^2 - (R_S + R_T)^2 > 0 \tag{47}$$

Further representing β_{CA} as the function of $\boldsymbol{q}_{S/T}$, one has:

$$\beta_{CA} = 4(\boldsymbol{q}_{S/T} \circ \boldsymbol{q}_{S/T} - 1) - (R_S + R_T)^2 > 0 \tag{48}$$

Equation (48) is exactly the collision avoidance constraint represented in terms of the dual quaternion $\boldsymbol{q}_{S/T}$.

6. Control of Proximity Maneuver

Control law design is the focus of spacecraft proximity maneuver research, which determines the tracking accuracy of the target, the completion of observation tasks, and the safety of the spacecraft. This paper designs a proportional–derivative-like control law, which incorporates the unknown disturbances estimated by the ESO and deals with the pose constraints using the APF method.

6.1. Maneuver Tracking Objective

The proximity maneuvering of service spacecraft is also a process of pose adjustment for the subsequent implementation of on-orbit operations. The objective of maneuver tracking is to make spacecraft autonomously transfer to the desired relative pose while satisfying observation and safety constraints. Depending on the relative pose required for subsequent missions, the service spacecraft keeps relatively stationary with the target spacecraft in the end.

The pose of the desired frame $o_D - x_D y_D z_D$ with respect to the target spacecraft is denoted by the dual quaternion $\boldsymbol{q}_{D/T}$, i.e., the desired state, which is defined as follows:

$$\boldsymbol{q}_{D/T} = q_{D/T} + \epsilon r^{T}_{D/T} q_{D/T}/2 \tag{49}$$

where the quaternions $q_{D/T}$ and $r^{T}_{D/T} = (0, \vec{r}^{T}_{D/T})$ denote the desired relative attitude and position, respectively, and $\vec{r}^{T}_{D/T}$ is the desired relative position vector observed in the $o_T - x_T y_T z_T$. The error dual quaternion $\boldsymbol{q}_E$ can be further determined as:

$$\boldsymbol{q}_E = \boldsymbol{q}^{*}_{D/T} \boldsymbol{q}_{S/T} = [\boldsymbol{q}^{*}_{D/T}] \circledast \boldsymbol{q}_{S/T} \tag{50}$$

The objective of maneuver tracking is to realize $\lim_{t \to +\infty} \boldsymbol{q}_{S/T} = \boldsymbol{q}_{D/T}$, i.e., $\lim_{t \to +\infty} \boldsymbol{q}_E = \mathbf{1}$, i.e., the unit dual quaternion, in the presence of unknown disturbances while the constraints are strictly satisfied.

6.2. APF Design

The artificial potential field method is effective to deal with constraints, and was initially aimed at obstacle avoidance planning for robots. It was developed and applied to design a control law for spacecraft rendezvous and docking [47], and generate proximity flight trajectories in the vicinity of space stations [48], etc. For a controlled system, one can define a scalar characteristic function, i.e., the APF, associated with state variables. The function has a minimum at the desired state, while it takes very large values in the undesired state set. By taking the negative gradient of the APF as the control action, the states of the system can be guided towards the desired state, exactly corresponding to the minimum of the APF, while avoiding falling into the state set formed by constraints. If the

APF is a convex function of state variables, the system will eventually reach and stabilize at the desired state with the control action. However, if the APF has multiple minima, the system will eventually stabilize at a certain state corresponding to one of its minima. Therefore, it is better to formulate an APF with a unique minimum.

The APF is generally designed as a combination of attractive and repulsive potential functions. The attractive potential function takes the desired state as the global minimum, and its negative gradient can drive the system state to the desired state. This paper defines the attractive potential function as follows:

$$V_{\mathrm{a}} = \mathrm{k_a} \Delta \boldsymbol{q} \circ \Delta \boldsymbol{q} \tag{51}$$

where $\mathrm{k_a} > 0$ is a constant coefficient, and $\Delta \boldsymbol{q} = \boldsymbol{q}_{\mathrm{E}} - \mathbf{1}$. The repulsive potential function increases as the relative pose approaches the constraint boundaries, at which the function is infinite. In this way, the motion state cannot cross the boundaries during proximity maneuvering, thus ensuring that the constraints are satisfied. This paper defines the repulsive potential function as follows:

$$V_{\mathrm{r}} = \mathrm{k_r} \Delta \boldsymbol{q} \circ \Delta \boldsymbol{q} (\beta_{\mathrm{FOV}}^{-1} + \beta_{\mathrm{CA}}^{-1}) \tag{52}$$

where $\mathrm{k_r} > 0$ is a constant coefficient. Combining Equations (51) and (52) yields the global APF:

$$V_{\mathrm{p}} = \mathrm{k_a} \Delta \boldsymbol{q} \circ \Delta \boldsymbol{q} + \mathrm{k_r} \Delta \boldsymbol{q} \circ \Delta \boldsymbol{q} (\beta_{\mathrm{FOV}}^{-1} + \beta_{\mathrm{CA}}^{-1}) \tag{53}$$

Due to the introduction of $\Delta \boldsymbol{q} \circ \Delta \boldsymbol{q}$ as a product term in the repulsive potential function, the global APF still has a minimum at $\boldsymbol{q}_{\mathrm{D/T}}$. Obviously, the global APF, V_{p}, satisfies the following: (1) for any $\boldsymbol{q}_{\mathrm{S/T}}$, there is $V_{\mathrm{p}} \geqslant 0$; (2) $V_{\mathrm{p}} = 0$ if and only if $\boldsymbol{q}_{\mathrm{S/T}} = \boldsymbol{q}_{\mathrm{D/T}}$.

Since $\nabla V_{\mathrm{p}} = \partial V_{\mathrm{p}} / \partial \boldsymbol{q}_{\mathrm{S/T}}$ is used in the subsequent control law design, it is calculated as follows:

$$\nabla V_{\mathrm{p}} = \frac{2V_{\mathrm{p}}}{\Delta \boldsymbol{q} \circ \Delta \boldsymbol{q}} [\boldsymbol{q}_{\mathrm{D/T}}^*]^{\mathrm{T}} \circledast \Delta \boldsymbol{q} - \mathrm{k_r} \Delta \boldsymbol{q} \circ \Delta \boldsymbol{q} \left(\frac{\nabla \beta_{\mathrm{FOV}}}{\beta_{\mathrm{FOV}}^2} + \frac{\nabla \beta_{\mathrm{CA}}}{\beta_{\mathrm{CA}}^2} \right) \tag{54}$$

where $\nabla \beta_{\mathrm{FOV}}$ and $\nabla \beta_{\mathrm{CA}}$ are as follows:

$$\begin{cases} \nabla \beta_{\mathrm{FOV}} = -2\mathrm{K}_{\vec{\mathrm{u}}} \circledast \boldsymbol{q}_{\mathrm{S/T}} + (\cot \theta)^2 \dfrac{4\boldsymbol{q}_{\mathrm{S/T}} - 2\beta_{\mathrm{T}} \mathrm{K}_{\vec{\mathrm{u}}} \circledast \boldsymbol{q}_{\mathrm{S/T}}}{\beta_{\mathrm{FOV}} + \beta_{\mathrm{T}} + \mathrm{z}_{\mathrm{N}'}} \\ \nabla \beta_{\mathrm{CA}} = 8\boldsymbol{q}_{\mathrm{S/T}} \end{cases} \tag{55}$$

To check whether the global APF, V_{p}, is convex or not, the Hessian matrix is further calculated:

$$\begin{aligned} \nabla^2 V_{\mathrm{p}} = {} & 2(\mathrm{k_a} + \mathrm{k_r}(\beta_{\mathrm{FOV}}^{-1} + \beta_{\mathrm{CA}}^{-1}))[\boldsymbol{q}_{\mathrm{D/T}}^*]^{\mathrm{T}}[\boldsymbol{q}_{\mathrm{D/T}}^*] \\ & + 2\mathrm{k_r} \Delta \boldsymbol{q} \circ \Delta \boldsymbol{q} (\beta_{\mathrm{FOV}}^{-3} \nabla \beta_{\mathrm{FOV}} (\nabla \beta_{\mathrm{FOV}})^{\mathrm{T}} + \beta_{\mathrm{CA}}^{-3} \nabla \beta_{\mathrm{CA}} (\nabla \beta_{\mathrm{CA}})^{\mathrm{T}}) \\ & - 2\mathrm{k_r}(\Xi + \Xi^{\mathrm{T}}) - \mathrm{k_r} \Delta \boldsymbol{q} \circ \Delta \boldsymbol{q} (\beta_{\mathrm{FOV}}^{-2} \nabla^2 \beta_{\mathrm{FOV}} + \beta_{\mathrm{CA}}^{-2} \nabla^2 \beta_{\mathrm{CA}}) \end{aligned} \tag{56}$$

where the matrix $\Xi = [\boldsymbol{q}_{\mathrm{D/T}}^*]^{\mathrm{T}} \circledast \Delta \boldsymbol{q} (\beta_{\mathrm{FOV}}^{-2} \nabla \beta_{\mathrm{FOV}} + \beta_{\mathrm{CA}}^{-2} \nabla \beta_{\mathrm{CA}})^{\mathrm{T}}$, and $\nabla^2 \beta_{\mathrm{FOV}}$ and $\nabla^2 \beta_{\mathrm{CA}}$ are the Hessian matrices of β_{FOV} and β_{CA} with respect to $\boldsymbol{q}_{\mathrm{S/T}}$, respectively. Note that the dual quaternions are treated as column vectors if necessary in Equations (54)–(56).

From Equation (56), it can be seen that the first term on the right side is a positive-definite matrix and the second is a positive-semi-definite matrix, while the last two matrices are indefinite. Since the two spacecraft are subject to the gravity of the Earth, the relative motion state representations are always finite magnitudes. Therefore, all scalar or matrix entries contained in $\nabla^2 V_{\mathrm{p}}$ are finite in the 6-DOF space defined by $\beta_{\mathrm{FOV}} > 0$ and $\beta_{\mathrm{CA}} > 0$. The first term on the right side in Equation (56) contains a constant coefficient $\mathrm{k_a}$, and the last two terms contain $\mathrm{k_r}$. If $\mathrm{k_a} \gg \mathrm{k_r}$, the matrix $\nabla^2 V_{\mathrm{p}}$ can be positive-definite, which guarantees that V_{p} is a convex function of $\boldsymbol{q}_{\mathrm{S/T}}$ and thus has a unique minimum. Therefore,

as long as the initial and desired relative poses satisfy the constraints and the control law is designed based on the global APF, $\beta_{\mathrm{FOV}} > 0$ and $\beta_{\mathrm{CA}} > 0$ can always be satisfied and the state $\boldsymbol{q}_{\mathrm{S/T}}$ can reach and stabilize at $\boldsymbol{q}_{\mathrm{D/T}}$.

6.3. Control Law Design

With the disturbances estimated by the ESO and the global APF based on the FOV constraint and collision avoidance. The proportional–derivative-like feedback control law with disturbance compensation is proposed to achieve the proximity maneuvering of service spacecraft and observation of the target. This is summarized in Proposition 2.

Proposition 2. *Considering the spacecraft proximity maneuver tracking system given by Equations (15) and (21) with unknown disturbances and pose constraints, we design a proportional–derivative-like feedback control input applied to service spacecraft as follows:*

$$\boldsymbol{f}_{\mathrm{C}}^{\mathrm{S}} = -\mathrm{k_p}\mathrm{vec}(\boldsymbol{q}_{\mathrm{S/T}}^{*}(\mathrm{E} \circledast \nabla V_{\mathrm{p}})) - \mathrm{k_d}(\mathrm{E} \circledast \boldsymbol{\omega}_{\mathrm{S/T}}^{\mathrm{S}}) + \boldsymbol{\omega}_{\mathrm{T/I}}^{\mathrm{S}} \times (\mathrm{J_E} \circledast \boldsymbol{\omega}_{\mathrm{T/I}}^{\mathrm{S}}) - \boldsymbol{f}_{\mathrm{G}}^{\mathrm{S}} - \mathrm{J_E} \circledast \hat{\boldsymbol{d}}^{\mathrm{S}} \quad (57)$$

where both $\mathrm{k_p} > 0$ *and* $\mathrm{k_d} > 0$ *are constant coefficients. Then, under control law (57), the relative pose of two spacecraft can converge and stabilize to the desired pose, i.e.,* $\lim_{t \to +\infty} \boldsymbol{q}_{\mathrm{S/T}} = \boldsymbol{q}_{\mathrm{D/T}}$ *and* $\lim_{t \to +\infty} \boldsymbol{\omega}_{\mathrm{S/T}}^{\mathrm{S}} = \mathbf{0}$. *Moreover, the FOV constraint and collision avoidance constraint are strictly obeyed during the whole proximity maneuver, i.e.,* $\beta_{\mathrm{FOV}} > 0$ *and* $\beta_{\mathrm{CA}} > 0$.

Proof of Proposition 2. According to the proof of Proposition 1, there exists a symmetric positive-definite matrix D for the estimated error of disturbances $\Delta\boldsymbol{d}$, such that $V_{\mathrm{d}} = \Delta\boldsymbol{d} \circ (\mathrm{D} \circledast \Delta\boldsymbol{d})$ satisfies $\dot{V}_{\mathrm{d}} \leqslant -V_{\mathrm{d}}$. Consider the following candidate Lyapunov function:

$$V(\boldsymbol{q}_{\mathrm{S/T}}, \boldsymbol{\omega}_{\mathrm{S/T}}^{\mathrm{S}}, \Delta\boldsymbol{d}) = 2\mathrm{k_p}V_{\mathrm{p}} + \boldsymbol{\omega}_{\mathrm{S/T}}^{\mathrm{S}} \circ ((\mathrm{EJE}) \circledast \boldsymbol{\omega}_{\mathrm{S/T}}^{\mathrm{S}})/2 + \mathrm{k_v}V_{\mathrm{d}} \quad (58)$$

where $\mathrm{EJE} = \mathrm{diag}(\mathrm{J_M}, \mathrm{J_m})$ is obviously a symmetric positive-definite matrix. Then, $\boldsymbol{\omega}_{\mathrm{S/T}}^{\mathrm{S}} \circ ((\mathrm{EJE}) \circledast \boldsymbol{\omega}_{\mathrm{S/T}}^{\mathrm{S}}) \geqslant 0$ holds for any $\boldsymbol{\omega}_{\mathrm{S/T}}^{\mathrm{S}}$. $\boldsymbol{\omega}_{\mathrm{S/T}}^{\mathrm{S}} \circ ((\mathrm{EJE}) \circledast \boldsymbol{\omega}_{\mathrm{S/T}}^{\mathrm{S}}) = 0$ if and only if $\boldsymbol{\omega}_{\mathrm{S/T}}^{\mathrm{S}} = \mathbf{0}$. Therefore, $V \geqslant 0$ holds for any $\boldsymbol{q}_{\mathrm{S/T}}$, $\boldsymbol{\omega}_{\mathrm{S/T}}^{\mathrm{S}}$, and $\Delta\boldsymbol{d}$. $V = 0$ if and only if $\boldsymbol{q}_{\mathrm{S/T}} = \boldsymbol{q}_{\mathrm{D/T}}$ and $\boldsymbol{\omega}_{\mathrm{S/T}}^{\mathrm{S}} = \Delta\boldsymbol{d} = \mathbf{0}$.

The time derivative of V is calculated as follows:

$$\begin{aligned} \dot{V} &= 2\mathrm{k_p}\dot{V}_{\mathrm{p}} + \boldsymbol{\omega}_{\mathrm{S/T}}^{\mathrm{S}} \circ ((\mathrm{EJE}) \circledast \dot{\boldsymbol{\omega}}_{\mathrm{S/T}}^{\mathrm{S}}) + \mathrm{k_v}\dot{V}_{\mathrm{d}} \\ &= 2\mathrm{k_p}\nabla V_{\mathrm{p}} \circ \dot{\boldsymbol{q}}_{\mathrm{S/T}} + (\mathrm{E} \circledast \boldsymbol{\omega}_{\mathrm{S/T}}^{\mathrm{S}}) \circ (\mathrm{J_E} \circledast \dot{\boldsymbol{\omega}}_{\mathrm{S/T}}^{\mathrm{S}}) + \mathrm{k_v}\dot{V}_{\mathrm{d}} \end{aligned} \quad (59)$$

Substituting Equations (15), (21), and (57) into Equation (59) yields:

$$\begin{aligned} \dot{V} = {} & \mathrm{k_p}\nabla V_{\mathrm{p}} \circ (\boldsymbol{q}_{\mathrm{S/T}}\boldsymbol{\omega}_{\mathrm{S/T}}^{\mathrm{S}}) + (\mathrm{E} \circledast \boldsymbol{\omega}_{\mathrm{S/T}}^{\mathrm{S}}) \circ (-\mathrm{k_p}\mathrm{vec}(\boldsymbol{q}_{\mathrm{S/T}}^{*}(\mathrm{E} \circledast \nabla V_{\mathrm{p}})) - \mathrm{k_d}(\mathrm{E} \circledast \boldsymbol{\omega}_{\mathrm{S/T}}^{\mathrm{S}}) \\ & + \boldsymbol{\omega}_{\mathrm{T/I}}^{\mathrm{S}} \times (\mathrm{J_E} \circledast \boldsymbol{\omega}_{\mathrm{T/I}}^{\mathrm{S}}) - \boldsymbol{\omega}_{\mathrm{S/I}}^{\mathrm{S}} \times (\mathrm{J_E} \circledast \boldsymbol{\omega}_{\mathrm{S/I}}^{\mathrm{S}}) + \mathrm{J_E} \circledast (\boldsymbol{\omega}_{\mathrm{S/T}}^{\mathrm{S}} \times \boldsymbol{\omega}_{\mathrm{S/I}}^{\mathrm{S}}) + \mathrm{J_E} \circledast \Delta\boldsymbol{d}) + \mathrm{k_v}\dot{V}_{\mathrm{d}} \end{aligned} \quad (60)$$

Regrouping some terms in Equation (60) can yield:

$$\begin{aligned} & \mathrm{k_p}\nabla V_{\mathrm{p}} \circ (\boldsymbol{q}_{\mathrm{S/T}}\boldsymbol{\omega}_{\mathrm{S/T}}^{\mathrm{S}}) + (\mathrm{E} \circledast \boldsymbol{\omega}_{\mathrm{S/T}}^{\mathrm{S}}) \circ (-\mathrm{k_p}\mathrm{vec}(\boldsymbol{q}_{\mathrm{S/T}}^{*}(\mathrm{E} \circledast \nabla V_{\mathrm{p}}))) \\ & = \mathrm{k_p}(\mathrm{E} \circledast \boldsymbol{\omega}_{\mathrm{S/T}}^{\mathrm{S}}) \circ (\boldsymbol{q}_{\mathrm{S/T}}^{*}(\mathrm{E} \circledast \nabla V_{\mathrm{p}})) + (\mathrm{E} \circledast \boldsymbol{\omega}_{\mathrm{S/T}}^{\mathrm{S}}) \circ (-\mathrm{k_p}\mathrm{vec}(\boldsymbol{q}_{\mathrm{S/T}}^{*}(\mathrm{E} \circledast \nabla V_{\mathrm{p}}))) \\ & = \mathrm{k_p}(\mathrm{E} \circledast \boldsymbol{\omega}_{\mathrm{S/T}}^{\mathrm{S}}) \circ \mathrm{sca}(\boldsymbol{q}_{\mathrm{S/T}}^{*}(\mathrm{E} \circledast \nabla V_{\mathrm{p}})) \\ & = \mathbf{0} \end{aligned} \quad (61)$$

and

$$\begin{aligned}
&(\mathrm{E} \circledast \boldsymbol{\omega}^{\mathrm{S}}_{\mathrm{S/T}}) \circ (\boldsymbol{\omega}^{\mathrm{S}}_{\mathrm{T/I}} \times (\mathrm{J_E} \circledast \boldsymbol{\omega}^{\mathrm{S}}_{\mathrm{T/I}}) - \boldsymbol{\omega}^{\mathrm{S}}_{\mathrm{S/I}} \times (\mathrm{J_E} \circledast \boldsymbol{\omega}^{\mathrm{S}}_{\mathrm{S/I}}) + \mathrm{J_E} \circledast (\boldsymbol{\omega}^{\mathrm{S}}_{\mathrm{S/T}} \times \boldsymbol{\omega}^{\mathrm{S}}_{\mathrm{S/I}})) \\
&= (\mathrm{E} \circledast \boldsymbol{\omega}^{\mathrm{S}}_{\mathrm{S/T}}) \circ (\mathrm{J_E} \circledast (\boldsymbol{\omega}^{\mathrm{S}}_{\mathrm{S/T}} \times \boldsymbol{\omega}^{\mathrm{S}}_{\mathrm{S/I}}) - \boldsymbol{\omega}^{\mathrm{S}}_{\mathrm{S/I}} \times (\mathrm{J_E} \circledast \boldsymbol{\omega}^{\mathrm{S}}_{\mathrm{S/T}}) - \boldsymbol{\omega}^{\mathrm{S}}_{\mathrm{S/T}} \times (\mathrm{J_E} \circledast \boldsymbol{\omega}^{\mathrm{S}}_{\mathrm{T/I}})) \\
&= (\mathrm{EJ} \circledast (\mathrm{E} \circledast \boldsymbol{\omega}^{\mathrm{S}}_{\mathrm{S/T}})) \circ (\boldsymbol{\omega}^{\mathrm{S}}_{\mathrm{S/T}} \times \boldsymbol{\omega}^{\mathrm{S}}_{\mathrm{S/I}}) - (\mathrm{E} \circledast (\mathrm{J_E} \circledast \boldsymbol{\omega}^{\mathrm{S}}_{\mathrm{S/T}})) \circ (\boldsymbol{\omega}^{\mathrm{S}}_{\mathrm{S/T}} \times \boldsymbol{\omega}^{\mathrm{S}}_{\mathrm{S/I}}) \\
&= ((\mathrm{EJE}) \circledast \boldsymbol{\omega}^{\mathrm{S}}_{\mathrm{S/T}}) \circ (\boldsymbol{\omega}^{\mathrm{S}}_{\mathrm{S/T}} \times (\boldsymbol{\omega}^{\mathrm{S}}_{\mathrm{S/I}} - \boldsymbol{\omega}^{\mathrm{S}}_{\mathrm{S/I}})) \\
&= \mathbf{0}
\end{aligned} \tag{62}$$

According to Equations (61) and (62), Equation (60) can be simplified as:

$$\begin{aligned}
\dot{V} &= (\mathrm{E} \circledast \boldsymbol{\omega}^{\mathrm{S}}_{\mathrm{S/T}}) \circ (-\mathrm{k_v}(\mathrm{E} \circledast \boldsymbol{\omega}^{\mathrm{S}}_{\mathrm{S/T}}) + \mathrm{J_E} \circledast \Delta\boldsymbol{d}) + \mathrm{k_p}\dot{V}_{\mathrm{d}} \\
&= -\mathrm{k_d}\boldsymbol{\omega}^{\mathrm{S}}_{\mathrm{S/T}} \circ \boldsymbol{\omega}^{\mathrm{S}}_{\mathrm{S/T}} + \boldsymbol{\omega}^{\mathrm{S}}_{\mathrm{S/T}} \circ (\mathrm{EJE} \circledast \Delta\boldsymbol{d}) + \mathrm{k_v}\dot{V}_{\mathrm{d}} \\
&\leqslant -\mathrm{k_d}\boldsymbol{\omega}^{\mathrm{S}}_{\mathrm{S/T}} \circ \boldsymbol{\omega}^{\mathrm{S}}_{\mathrm{S/T}} + \boldsymbol{\omega}^{\mathrm{S}}_{\mathrm{S/T}} \circ (\mathrm{EJE} \circledast \Delta\boldsymbol{d}) - \mathrm{k_v}\Delta\boldsymbol{d} \circ (\mathrm{D} \circledast \Delta\boldsymbol{d})
\end{aligned} \tag{63}$$

The column vector $\vec{x}_1$ is constructed by arranging entries of the real and dual parts of $\boldsymbol{\omega}^{\mathrm{S}}_{\mathrm{S/T}}$ in sequence, respectively. The same operations on $\Delta\boldsymbol{d}$ are used to construct $\vec{x}_2$. Equation (63) can be equivalently transformed into:

$$\dot{V} \leqslant -\begin{bmatrix}\vec{x}_1\\ \vec{x}_2\end{bmatrix}^{\mathrm{T}} \begin{bmatrix}\mathrm{k_d}\mathrm{I}_{8\times 8} & -\mathrm{EJE}/2\\ -\mathrm{EJE}/2 & \mathrm{k_v}\mathrm{D}\end{bmatrix} \begin{bmatrix}\vec{x}_1\\ \vec{x}_2\end{bmatrix} = -\vec{X}\mathrm{H}\vec{X} \tag{64}$$

where $\mathrm{I}_{8\times 8}$ is a square 8×8 identity matrix. It follows from the matrix theory that one can choose suitable coefficients $\mathrm{k_d}$ and $\mathrm{k_v}$ such that H is a positive-definite matrix and thus $\dot{V} \leqslant 0$ holds. $\dot{V} = 0$ if and only if $\boldsymbol{\omega}^{\mathrm{S}}_{\mathrm{S/T}} = \Delta\boldsymbol{d} = \mathbf{0}$.

Since $V \geqslant 0$ and $\dot{V} \leqslant 0$, V and the related quantities V_{p}, $\boldsymbol{q}_{\mathrm{S/T}}$, and $\boldsymbol{\omega}^{\mathrm{S}}_{\mathrm{S/T}}$ are all bounded and $\lim_{t\to+\infty} V(t)$ exists. V_{p} being bounded indicates that $\beta_{\mathrm{FOV}} \neq 0$ and $\beta_{\mathrm{CA}} \neq 0$ always hold when $t \geqslant 0$. Therefore, as long as the initial relative pose satisfies the constraints, i.e., $\beta_{\mathrm{FOV}}(t=0) > 0$ and $\beta_{\mathrm{CA}}(t=0) > 0$, for the their continuity over time in this system, $\beta_{\mathrm{FOV}}(t>0) > 0$ and $\beta_{\mathrm{CA}}(t>0) > 0$ hold, i.e., the relative pose of the two spacecraft will always satisfy the observation and collision avoidance constraints. After integrating both sides of Equation (63) and taking the limit with $t \to +\infty$, in view of the boundedness of $V(0)$ and existence of $\lim_{t\to+\infty} V(t)$, $\lim_{t\to+\infty} \int_0^t (\boldsymbol{\omega}^{\mathrm{S}}_{\mathrm{S/T}} \circ \boldsymbol{\omega}^{\mathrm{S}}_{\mathrm{S/T}})\mathrm{d}t$ exists. Then, there is $\lim_{t\to+\infty} \boldsymbol{\omega}^{\mathrm{S}}_{\mathrm{S/T}} = \mathbf{0}$ according to Barbalat's lemma, and further, $\lim_{t\to+\infty} \boldsymbol{\omega}^{\mathrm{S}}_{\mathrm{S/I}} = \boldsymbol{\omega}^{\mathrm{S}}_{\mathrm{T/I}}$. Based on Equation (21), the boundedness of $\boldsymbol{\omega}^{\mathrm{S}}_{\mathrm{S/I}}$, $\boldsymbol{d}^{\mathrm{S}}$, V_{p}, $\boldsymbol{q}_{\mathrm{S/T}}$, and $\boldsymbol{\omega}^{\mathrm{S}}_{\mathrm{S/T}}$ leads to $\dot{\boldsymbol{\omega}}^{\mathrm{S}}_{\mathrm{S/T}}$ being bounded. Finding the time derivative of Equation (21), since $\dot{\boldsymbol{\omega}}^{\mathrm{S}}_{\mathrm{S/T}}$ is bounded and $\sqrt{\boldsymbol{\alpha} \circ \boldsymbol{\alpha}} \leqslant \mathrm{C}$, $\ddot{\boldsymbol{\omega}}^{\mathrm{S}}_{\mathrm{S/T}}$ is also bounded. It can be determined that $\lim_{t\to+\infty} \dot{\boldsymbol{\omega}}^{\mathrm{S}}_{\mathrm{S/T}} = \mathbf{0}$ using the Barbalat's lemma. Finally, combining dynamics Equation (21) and control input Equation (57), $\lim_{t\to+\infty} \boldsymbol{\omega}^{\mathrm{S}}_{\mathrm{S/T}} = \mathbf{0}$, $\lim_{t\to+\infty} \dot{\boldsymbol{\omega}}^{\mathrm{S}}_{\mathrm{S/T}} = \mathbf{0}$, and $\lim_{t\to+\infty} \Delta\boldsymbol{d} = \mathbf{0}$ are used to obtain $\lim_{t\to+\infty} \mathrm{vec}(\boldsymbol{q}^{*}_{\mathrm{S/T}}(\mathrm{E} \circledast \nabla V_{\mathrm{p}})) = \mathbf{0}$, through which it is further derived that $\lim_{t\to+\infty} \boldsymbol{q}_{\mathrm{S/T}} = \boldsymbol{q}_{\mathrm{D/T}}$. □

A block diagram of the proportional–derivative-like feedback control system is shown in Figure 4.

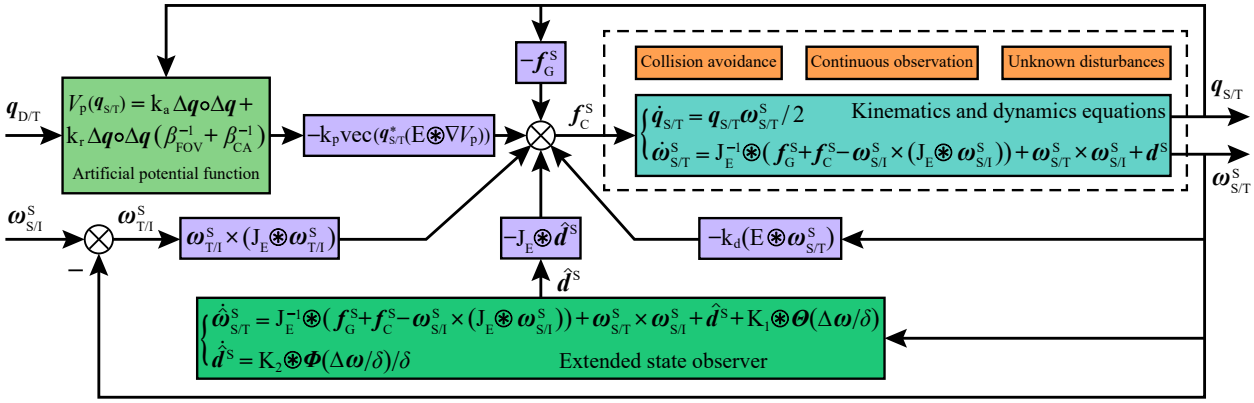

Figure 4. Diagram of proximity maneuver control scheme.

Remark 3. *Proposition 2 indicates that ESO-based pose-constrained tracking control law (57) is able to make service spacecraft safely approach and observe noncooperative targets through proximity maneuvers. Stable hovering of the two spacecraft can ultimately be achieved even in the presence of unknown disturbances.*

7. Numerical Simulations and Analyses

This paper verifies the performance of the proposed ESO and control scheme using numerical simulations. The simulation scenario is as follows: the service spacecraft carrying the optical camera reaches proximity to the noncooperative target spacecraft from a distance through pose maneuvering along with the observation of it, and eventually achieves a position relatively stationary to the target. The target spacecraft operates along a standard Keplerian orbit, whose altitude of perigee and apogee are 400 km and 600 km, respectively, and the corresponding orbital elements are shown in Table 1. In addition, the attitude of the target is Earth-oriented, with one of its surfaces being maintained towards the Earth. Therefore, the rotation angular velocity of the target is equal to its orbital angular velocity.

Table 1. The orbital elements of the target spacecraft.

Orbital Element Parameters	Numerical Magnitude
Semi-major axis (km)	6878.1366
Eccentricity (-)	0.01454
Inclination (deg)	45
Argument of periapsis (deg)	90
Longitude of ascending node (deg)	60
True anomaly at initial time (deg)	0

At the start, the camera is oriented exactly towards the target spacecraft. The initial relative position vector and attitude quaternion of the service spacecraft to the target are $\vec{r}^{\,\mathrm{T}}_{\mathrm{S/T},0} = (-158.4, -211.2, 77)^{\mathrm{T}}$ m and $q_{\mathrm{S/T},0} = (0.6, (-0.64, 0.48, 0)^{\mathrm{T}})$, respectively. Thenitial relative linear and angular velocity vectors are $\dot{\vec{r}}^{\,\mathrm{T}}_{\mathrm{S/T},0} = (0.02, 0.03, -0.015)^{\mathrm{T}}$ m/s and $\vec{\omega}^{\,\mathrm{T}}_{\mathrm{S/T},0} = (0.08, -0.06, 0.05)^{\mathrm{T}}$ deg/s, respectively. The initial position vector and attitude quaternion of the target spacecraft relative to the $O-XYZ$ frame are $\vec{r}^{\,\mathrm{I}}_{\mathrm{T/I},0} = (-4150.744, 2396.433, 4792.866)^{\mathrm{T}}$ km and $q_{\mathrm{T/I},0} = (0.2391, (0.3696, -0.0990, 0.8924)^{\mathrm{T}})$, respectively. The corresponding linear and angular velocity vectors are $\dot{\vec{r}}^{\,\mathrm{I}}_{\mathrm{T/I},0} = (-3862.052, -6689.269, 0)^{\mathrm{T}}$ m/s and $\vec{\omega}^{\,\mathrm{I}}_{\mathrm{T/I},0} = (0.03998, -0.02308, 0.04617)^{\mathrm{T}}$ deg/s, respectively. At the end of the proximity maneuver, the desired relative position vector and attitude quaternion of the service spacecraft to the target are $\vec{r}^{\,\mathrm{T}}_{\mathrm{D/T}} = (50, 0, 0)^{\mathrm{T}}$ m and $q_{\mathrm{D/T}} = (\sqrt{2}/2, (0, -\sqrt{2}/2, 0)^{\mathrm{T}})$, respectively, and both the desired relative linear and angular velocity are 0. The mass, moment of inertia, and sphere envelope radius of the service spacecraft are $\mathrm{m} = 60$ kg, $\mathrm{M} = \mathrm{diag}(15.6, 10.8, 11.5)$ kg·m^2, and $\mathrm{R_S} = 2.1$ m, respectively. The sphere envelope radius of the target spacecraft is

$R_T = 1.5$ m. The parameters related to the camera are $\theta = 45$ deg and $z_N = 1.2$ m. The unknown integrated disturbances $\boldsymbol{d}^S = J_E^{-1} \circledast \boldsymbol{f}_D^S - \boldsymbol{q}_{S/T}^* \dot{\boldsymbol{\omega}}_{T/I}^T \boldsymbol{q}_{S/T}$, which result from $\boldsymbol{f}_D^S = (0, \vec{f}_D^S) + \epsilon(0, \vec{\tau}_D^S)$ and $\dot{\boldsymbol{\omega}}_{T/I}^T$, where $\vec{f}_D^S$ and $\vec{\tau}_D^S$ are space disturbance forces and moments applied to the service spacecraft, respectively, and $\dot{\boldsymbol{\omega}}_{T/I}^T$ is related to angular and linear acceleration of the target spacecraft. Space disturbance forces $\vec{f}_D^S$ are induced by J_2 perturbation, atmospheric drag, solar light pressure, three-body gravity perturbation, etc. Since the J_2 perturbation has a significant advantage over other perturbations, $\vec{f}_D^S$ is divided into two parts, i.e., J_2 perturbation $\vec{f}_{J_2}^S$ and other minimal perturbations $\vec{f}_O^S$. Then $\vec{f}_D^S = \vec{f}_{J_2}^S + \vec{f}_O^S$, and $\vec{f}_{J_2}^S$ can be transformed from $\vec{f}_{J_2}^I$, which is given by [49]:

$$\vec{f}_{J_2}^I = -\frac{3\mu m J_2 r_E^2}{2\|\vec{r}_{S/I}^I\|^4} \begin{bmatrix} \left(1 - 5(\frac{z_{S/I}^I}{\|\vec{r}_{S/I}^I\|})^2\right) \frac{x_{S/I}^I}{\|\vec{r}_{S/I}^I\|} \\ \left(1 - 5(\frac{z_{S/I}^I}{\|\vec{r}_{S/I}^I\|})^2\right) \frac{y_{S/I}^I}{\|\vec{r}_{S/I}^I\|} \\ \left(3 - 5(\frac{z_{S/I}^I}{\|\vec{r}_{S/I}^I\|})^2\right) \frac{z_{S/I}^I}{\|\vec{r}_{S/I}^I\|} \end{bmatrix} \tag{65}$$

where $J_2 = 1.0826355 \times 10^{-3}$, r_E is Earth's mean equatorial radius, and $\vec{r}_{S/I}^I = [x_{S/I}^I, y_{S/I}^I, z_{S/I}^I]^T$ represents the position vectors of the service spacecraft in the $O - XYZ$ frame. Since other perturbations are very small, their short-term impacts are very limited. Thus, $\vec{f}_O^S$ is modeled with reference to gravity as follows:

$$\vec{f}_O^S = mg \begin{bmatrix} 3.2 \\ 5.5 \\ 8.6 \end{bmatrix} \times 10^{-6} \tag{66}$$

where g is the local gravitational acceleration of the service spacecraft. Although Equation (66) is not an exact model, it reflects the correct order of magnitude of other perturbations. Space disturbance moments $\vec{\tau}_D^S$ are induced by atmospheric drag, solar radiation, terrestrial magnetism, etc. They are related not only to the positions, velocities, and space environments, but also to the characteristics, of the service spacecraft, such as the shape, material, mass distribution, and area–mass ratio. Therefore, it is extremely difficult and complex to establish a model for $\vec{\tau}_D^S$. However, the order of magnitude of different disturbance moments on near-Earth spacecraft is 10^{-4} N·m in practice. To simply the simulation, $\vec{\tau}_D^S$ is modeled as a sine function, a cosine function, and their combination with the same cycle of change as its orbit. The specific expressions of $\vec{\tau}_D^S$ are as follows:

$$\vec{\tau}_D^S = \begin{bmatrix} 7.2(\sin(v) + \cos(v)) \\ 8.1\cos(v) \\ 9.5\sin(v) \end{bmatrix} \times 10^{-4} \text{ N·m} \tag{67}$$

where v is a true anomaly. Although Equation (67) is not theoretically analyzed, it is in line with the real situation in terms of the order of magnitude and is sufficient to verify the proposed algorithm. $\dot{\boldsymbol{\omega}}_{T/I}^T$ represents the unknown maneuver accelerations of the target spacecraft. Using the transformation, $\boldsymbol{\omega}_{T/I}^T = \boldsymbol{q}_{T/I}^* \boldsymbol{\omega}_{T/I}^I \boldsymbol{q}_{T/I}$, $\dot{\boldsymbol{\omega}}_{T/I}^T$ can be calculated as follows:

$$\dot{\boldsymbol{\omega}}_{T/I}^T = \boldsymbol{q}_{T/I}^* (\dot{\boldsymbol{\omega}}_{T/I}^I + \boldsymbol{\omega}_{T/I}^I \times \boldsymbol{\omega}_{T/I}^I) \boldsymbol{q}_{T/I} = \boldsymbol{q}_{T/I}^* \dot{\boldsymbol{\omega}}_{T/I}^I \boldsymbol{q}_{T/I} \tag{68}$$

where $\dot{\boldsymbol{\omega}}_{T/I}^I = \dot{\omega}_{T/I}^I + \epsilon(\dot{r}_{T/I}^I + \dot{r}_{T/I}^I \times \omega_{T/I}^I + r_{T/I}^I \times \dot{\omega}_{T/I}^I)$, $r_{T/I}^I = (0, \vec{r}_{T/I}^I)$, $\omega_{T/I}^I = (0, \vec{\omega}_{T/I}^I)$, $\vec{r}_{T/I}^I$ and $\vec{\omega}_{T/I}^I$ are the position and angular velocity vectors of the target spacecraft relative to the $O - XYZ$ frame, respectively. According to the orbital elements and Earth-oriented attitude of the target, one can obtain $\vec{r}_{T/I}^I$, $\dot{\vec{r}}_{T/I}^I$, $\ddot{\vec{r}}_{T/I}^I$, $\omega_{T/I}^I$, and $\dot{\omega}_{T/I}^I$. Based on the above analysis, the integrated disturbances $\boldsymbol{d}^S$ can be simulated as realistically as possible to verify the performance of the proposed ESO and control scheme. In the ESO, both the

initial values of $\hat{\boldsymbol{\omega}}_{S/T}^{S}$ and $\hat{\boldsymbol{d}}^{S}$ are assigned by $\mathbf{0}$. The other parameters can be divided into two groups, i.e., the parameters of the ESO and control law. In the ESO, these values affect the convergence rate of disturbance estimation errors and can be chosen according to Proposition 1 as follows: $\kappa_1 = 0.7$, $\kappa_2 = 0.8$, $\delta = 0.001$, $k_{11} = \cdots = k_{14} = 1.0 \times 10^{-4}$, $k_{15} = \cdots = k_{18} = 1.5 \times 10^{-3}$, $k_{21} = \cdots = k_{24} = 1.6 \times 10^{-9}$, $k_{25} = \cdots = k_{28} = 5.6 \times 10^{-7}$. In the control law, the parameters of the APF are $k_a = 0.75$ and $k_r = 2.5 \times 10^{-5}$, which satisfies $k_a \gg k_r$. The parameters of the proportional–derivative-like feedback control law are similar to the PD controller and can be chosen according to Proposition 2 as follows: $k_p = 0.005$ and $k_d = 2$. In addition, considering the limitations of actuator capabilities, the torque and force that can be provided on each axis of the service spacecraft body frame are limited to $[-2, 2]$ mN·m and $[-750, 750]$ mN [50], respectively. The evolution of the absolute and relative translation and rotational dynamics is propagated by the high-precision fourth-order Runge–Kutta algorithm. The numerical simulation results are shown in Figures 5–14.

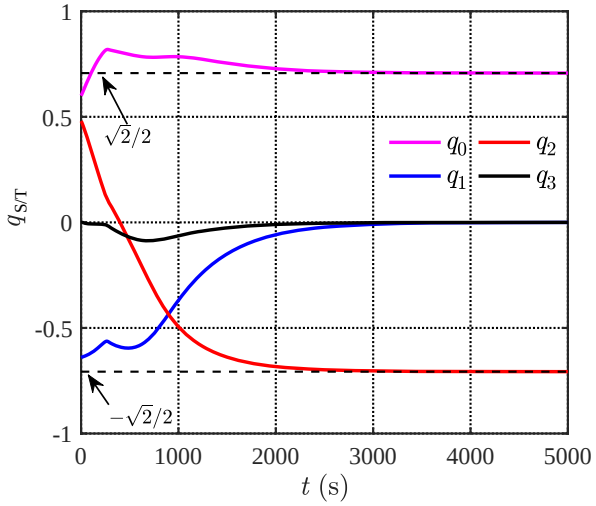

Figure 5. Relative attitude quaternions.

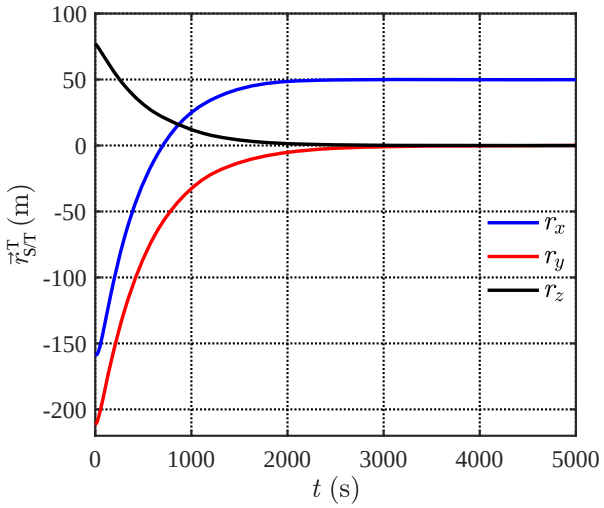

Figure 6. Relative positions.

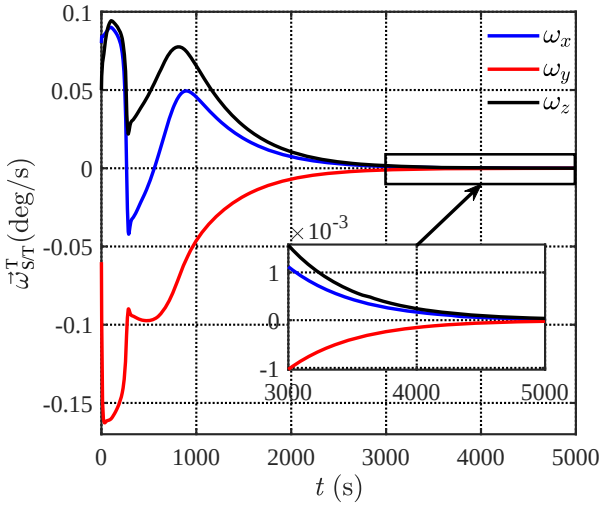

Figure 7. Relative angular velocities.

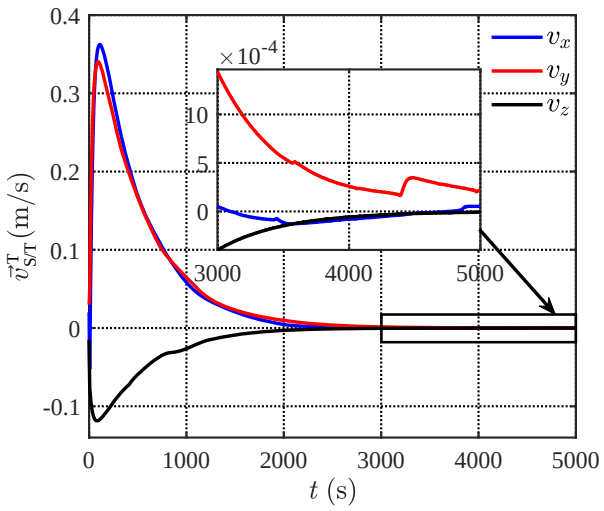

Figure 8. Relative linear velocities.

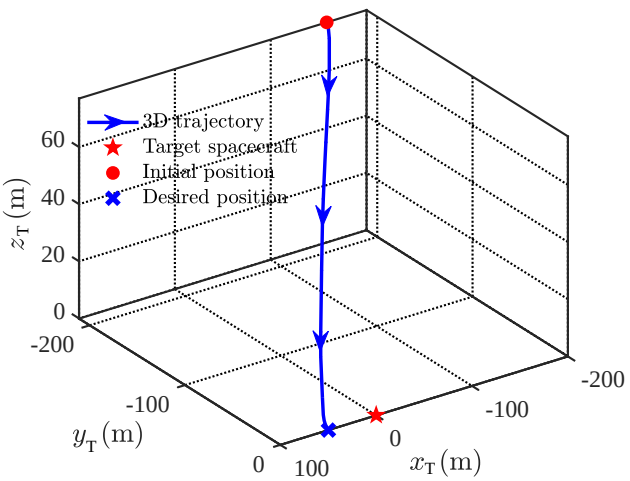

Figure 9. Three-dimensional trajectory of service spacecraft in $o_{\mathrm{T}} - x_{\mathrm{T}} y_{\mathrm{T}} z_{\mathrm{T}}$ frame.

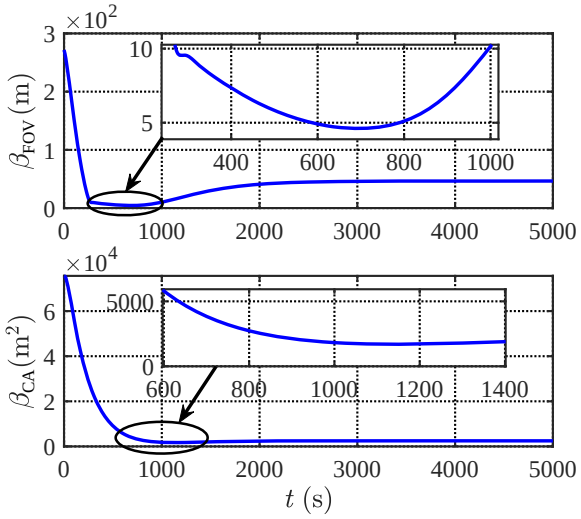

Figure 10. Constraint variables β_{FOV} and β_{CA}.

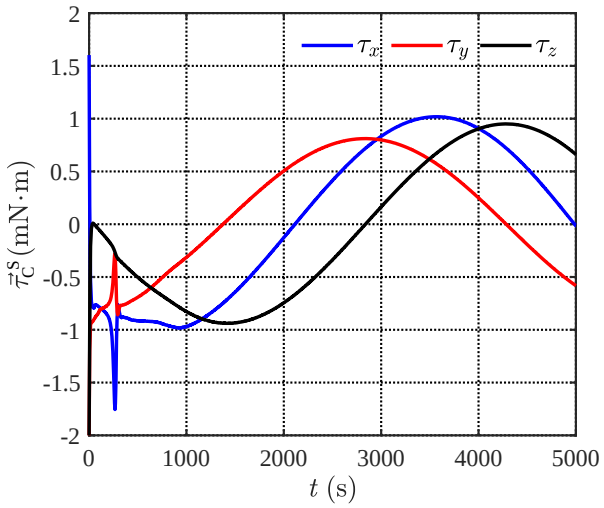

Figure 11. Active control torque on the service spacecraft.

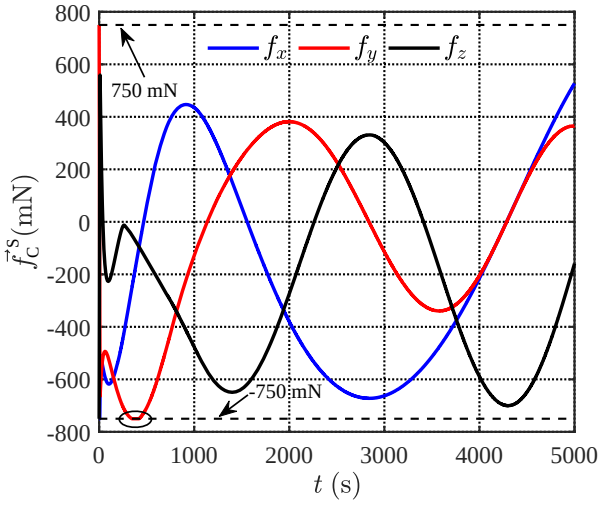

Figure 12. Active control force on the service spacecraft.

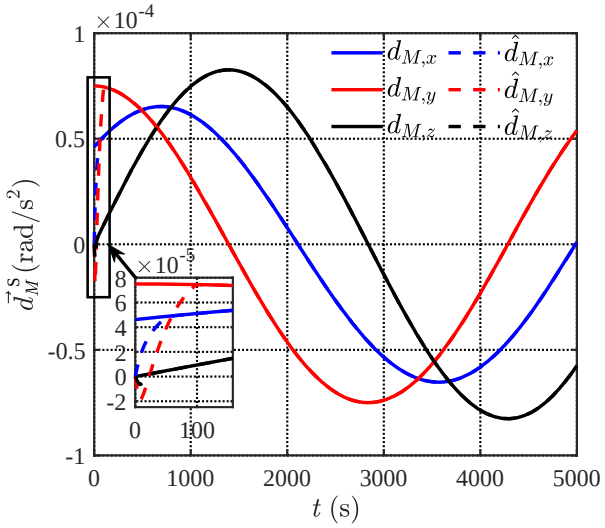

Figure 13. ESO-based estimations of angular acceleration disturbances.

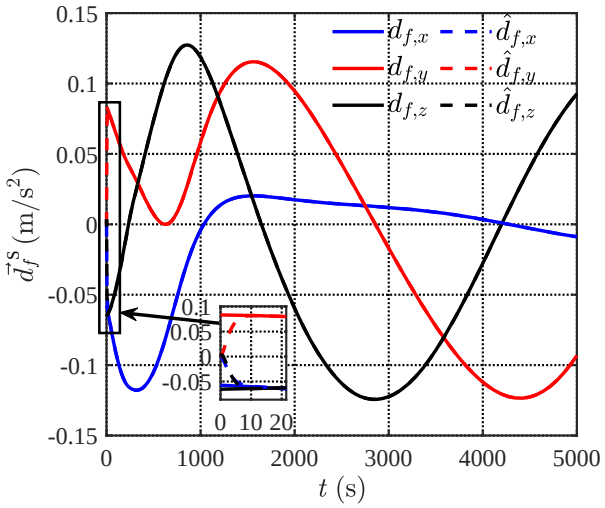

Figure 14. ESO-based estimations of linear acceleration disturbances.

Figures 5 and 7 show the changes in the relative attitude quaternions and angular velocities of the service spacecraft to the target, respectively. It can be seen that the service spacecraft adjusts its attitude significantly within 3000 s of the beginning of the proximity maneuver, and finally converges to the desired attitude at about 5000 s after slow regulation. Figures 6 and 8 show the changes in the relative positions and linear velocities, respectively, and indicate that the service spacecraft can reach the vicinity of the desired position within 3000 s. It further conducts slight adjustments and finally coincides with the desired position at about 5000 s. The good synchronization and coordination of the attitude and position changes are attributed to the integrated model based on the dual quaternions and control design. From the perspective of control performance, the two components of the relative attitude quaternion, i.e., q_0 and q_3, exhibit a slight overshoot, while the other two components, i.e., q_1 and q_2, and the three components of the relative position, i.e., r_x, r_y, and r_z, show no overshoot, indicating that the pose changes smoothly. Table 2 lists the control errors of the relative attitude quaternion, position, angular velocity, and linear velocity at 3000 s, 4000 s, and 5000 s, respectively. From Table 2, we can see that the service spacecraft closely approaches the desired pose at about 3000 s, and the control errors of both relative pose and velocity subsequently decrease further. The steady-state error magnitude of the relative attitude and the relative angular and linear velocity can reach 10^{-5}. The steady-state errors of the relative position are slightly larger, but still within

a reasonable range. The relative pose and velocity changes demonstrated in Figures 5–8 illustrate that the designed APF can effectively perform proximity maneuver planning, and the proposed control law has high tracking accuracy. The three-dimensional motion trajectory in Figure 9 indicates that the service spacecraft aims at the desired position, and approaches it almost in a straight line, which also indicates that there is no overshoot in the position control. In the early stage of maneuvering ($0 \sim 3000$ s), the changes in the angle of view are significant with the variations in the relative position. Therefore, the service spacecraft needs to adjust its attitude quickly to avoid losing observation of the target. Once the service spacecraft reaches the vicinity of the desired position, the distance between the two spacecraft will not change much anymore; thus, it is able to maintain observation with slight attitude regulations. The variations in β_{FOV} and β_{CA} in Figure 10 further explain this process. The attitude is quickly rotated to meet the FOV constraint during the service spacecraft approaching the desired position within 2000 s. Figure 10 also shows that the constraint variables β_{FOV} and β_{CA} are always greater than 0, indicating that the service spacecraft can observe the target and avoid collision in the entire process. Therefore, the AFP effectively deals with the constraints of the proximity maneuver. Figures 11 and 12 give the changes in active control torque and force, respectively, both of which do not exceed the set limits. Their synergistic effects make the relative pose changes in the service spacecraft to the target consistent with the need for real-time visual observation. The relative pose is stabilized at the desired value, but the input torque and force still cannot be zero due to continuously tracking the target spacecraft. Figures 13 and 14 show the estimations of the angular and linear acceleration of unknown integrated disturbances by the ESO, respectively. Although the estimation errors are significant at the start, the ESO is still able to estimate and keep tracking unknown angular and linear accelerations with high accuracy after 100 s and 20 s, respectively. It can be concluded that the designed STA-based ESO has good performance and achieves the stable tracking of unknown disturbances in a finite period of time. It is of great significance to obtain unknown disturbances for the control of proximity maneuvering, because effective compensations of disturbances in the control law can offset their influences on relative pose motion, thereby improving tracking accuracy.

Table 2. The control errors of relative poses and velocities at different time points.

Time Points	3000 s	4000 s	5000 s
Errors of $q_{\mathrm{S/T}}$ (-)	$(3.32, (-8.75, 3.39, -1.49)^{\mathrm{T}}) \times 10^{-3}$	$(5.18, (-12.9, 5.20, -2.33)^{\mathrm{T}}) \times 10^{-4}$	$(9.69, (-17.9, 9.70, 0.616)^{\mathrm{T}}) \times 10^{-5}$
Errors of $\vec{r}^{\mathrm{T}}_{\mathrm{S/T}}$ (m)	$(-0.0437, -0.8839, 0.1386)^{\mathrm{T}}$	$(-0.1197, -0.2294, -0.0345)^{\mathrm{T}}$	$(-0.1405, 0.0221, -0.0598)^{\mathrm{T}}$
Errors of $\vec{\omega}^{\mathrm{T}}_{\mathrm{S/T}}$ (deg/s)	$(1.12, -1.03, 1.57)^{\mathrm{T}} \times 10^{-3}$	$(1.69, -1.53, 2.42)^{\mathrm{T}} \times 10^{-4}$	$(2.09, -2.30, 3.68)^{\mathrm{T}} \times 10^{-5}$
Errors of $\vec{v}^{\mathrm{T}}_{\mathrm{S/T}}$ (m/s)	$(0.509, 14.3, -3.96)^{\mathrm{T}} \times 10^{-4}$	$(-7.89, 25.8, -5.52)^{\mathrm{T}} \times 10^{-5}$	$(5.36, 22.3, -0.681)^{\mathrm{T}} \times 10^{-5}$

In conclusion, these numerical simulation results show that the 6-DOF pose tracking control scheme for proximity maneuvering proposed in this paper has high accuracy, satisfies the requirements of the proximity observation task, and effectively avoids collision for safety.

8. Conclusions

This paper proposes an ESO-based pose-constrained control scheme for service spacecraft proximity maneuvering, which is used to track and observe a noncooperative target, and performs simulation verifications as well. Relative kinematics and dynamics equations with unknown disturbances by dual quaternion representations can effectively incorporate the pose-coupled characteristics of the proximity maneuver system in a simple and compact form. The designed STA-based ESO achieves high-accuracy estimations of unknown disturbances in a finite time. Therefore, the negative effects of disturbances can be eliminated by using their estimated values as compensations in the control law. The two constraint models represented by the relative pose dual quaternions can effectively characterize the

requirements of real-time observations for missions and collision avoidance for safety. A global APF consisting of an attractive and a repulsive potential function is designed using the constraint models. When the coefficient of the attractive potential function is much greater than that of the repulsive potential function, the global APF possesses a unique minimum in the constraint space, which is the key to achieving the desired pose. The proportional–derivative-like feedback control law is developed with estimated disturbances and an APF. The law is able to drive the service spacecraft to continuously observe the target spacecraft in real time through proximity maneuvering and ultimately achieve stable tracking with the desired pose.

Author Contributions: Conceptualization, Y.Z. and L.F.; methodology, M.Z.; software, X.W.; validation, M.Z.; formal analysis, X.W.; investigation, M.Z.; resources, Y.Z.; data curation, X.W.; writing—original draft preparation, M.Z.; writing—review and editing, M.Z.; visualization, M.Z.; supervision, Y.Z.; project administration, L.F.; funding acquisition, L.F. All authors have read and agreed to the published version of the manuscript.

Funding: This research was funded by the Intelligent Aerospace System Leading Innovation Team Program of Zhejiang (Grant No. 2022R01003).

Data Availability Statement: The original contributions presented in the study are included in the article, further inquiries can be directed to the corresponding author.

Acknowledgments: The authors are grateful to the reviewers for their constructive comments, which improved the paper quality.

Conflicts of Interest: The authors declare no conflicts of interest.

References

1. Wilde, M.; Clark, C.; Romano, M. Historical survey of kinematic and dynamic spacecraft simulators for laboratory experimentation of on-orbit proximity maneuvers. *Prog. Aerosp. Sci.* **2019**, *110*, 100552. [CrossRef]
2. Wang, L.; Guo, Y.; Ma, G.; Zhang, H. Artificial potential function based spacecraft proximity maneuver 6-DOF control under multiple pyramid-type constraints. *ISA Trans.* **2022**, *126*, 316–325. [CrossRef] [PubMed]
3. Li, W.J.; Cheng, D.Y.; Liu, X.G.; Wang, Y.B.; Shi, W.H.; Tang, Z.X.; Gao, F.; Zeng, F.M.; Chai, H.Y.; Luo, W.B.; et al. On-orbit service (OOS) of spacecraft: A review of engineering developments. *Prog. Aerosp. Sci.* **2019**, *108*, 32–120. [CrossRef]
4. Guo, Y.; Zhang, D.; Li, A.J.; Song, S.; Wang, C.Q.; Liu, Z. Finite-time control for autonomous rendezvous and docking under safe constraint. *Aerosp. Sci. Technol.* **2021**, *109*, 106380. [CrossRef]
5. Romano, M.; Friedman, D.A.; Shay, T.J. Laboratory experimentation of autonomous spacecraft approach and docking to a collaborative target. *J. Spacecr. Rocket.* **2007**, *44*, 164–173. [CrossRef]
6. Zappulla, R.; Virgili-Llop, J.; Zagaris, C.; Park, H.; Romano, M. Dynamic air-bearing hardware-in-the-loop testbed to experimentally evaluate autonomous spacecraft proximity maneuvers. *J. Spacecr. Rocket.* **2017**, *54*, 825–839. [CrossRef]
7. Yoshida, K. Engineering Test Satellite VII flight experiments for space robot dynamics and control: Theories on laboratory test beds ten years ago, now in orbit. *Int. J. Robot. Res.* **2003**, *22*, 321–335. [CrossRef]
8. McCamish, S.B.; Romano, M.; Nolet, S.; Edwards, C.M.; Miller, D.W. Flight testing of multiple-spacecraft control on SPHERES during close-proximity operations. *J. Spacecr. Rocket.* **2009**, *46*, 1202–1213. [CrossRef]
9. Dong, H.; Hu, Q.; Liu, Y.; Akella, M.R. Adaptive pose tracking control for spacecraft proximity operations under motion constraints. *J. Guid. Control Dyn.* **2019**, *42*, 2258–2271. [CrossRef]
10. Zhang, Z.; Deng, L.; Feng, J.; Chang, L.; Li, D.; Qin, Y. A survey of precision formation relative state measurement technology for distributed spacecraft. *Aerospace* **2022**, *9*, 362. [CrossRef]
11. Vela, C.; Fasano, G.; Opromolla, R. Pose determination of passively cooperative spacecraft in close proximity using a monocular camera and AruCo markers. *Acta Astronaut.* **2022**, *201*, 22–38. [CrossRef]
12. Opromolla, R.; Fasano, G.; Rufino, G.; Grassi, M. A review of cooperative and uncooperative spacecraft pose determination techniques for close-proximity operations. *Prog. Aerosp. Sci.* **2017**, *93*, 53–72. [CrossRef]
13. Wang, X.; Wang, Z.; Zhang, Y. Stereovision-based relative states and inertia parameter estimation of noncooperative spacecraft. *Proc. Inst. Mech. Eng. Part G J. Aerosp. Eng.* **2019**, *233*, 2489–2502. [CrossRef]
14. Pasqualetto Cassinis, L.; Fonod, R.; Gill, E. Review of the robustness and applicability of monocular pose estimation systems for relative navigation with an uncooperative spacecraft. *Prog. Aerosp. Sci.* **2019**, *110*, 100548. [CrossRef]
15. Pasqualetto Cassinis, L.; Menicucci, A.; Gill, E.; Ahrns, I.; Sanchez-Gestido, M. On-ground validation of a CNN-based monocular pose estimation system for uncooperative spacecraft: Bridging domain shift in rendezvous scenarios. *Acta Astronaut.* **2022**, *196*, 123–138. [CrossRef]

16. Capuano, V.; Kim, K.; Harvard, A.; Chung, S.J. Monocular-based pose determination of uncooperative space objects. *Acta Astronaut.* **2020**, *166*, 493–506. [CrossRef]
17. Li, Y.; Wang, Y.; Xie, Y. Using consecutive point clouds for pose and motion estimation of tumbling non-cooperative target. *Adv. Space Res.* **2019**, *63*, 1576–1587. [CrossRef]
18. Kang, G.; Zhang, Q.; Wu, J.; Zhang, H. Pose estimation of a non-cooperative spacecraft without the detection and recognition of point cloud features. *Acta Astronaut.* **2021**, *179*, 569–580. [CrossRef]
19. Guo, W.; Hu, W.; Liu, C.; Lu, T. Pose initialization of uncooperative spacecraft by template matching with sparse point cloud. *J. Guid. Control Dyn.* **2021**, *44*, 1707–1720. [CrossRef]
20. Pesce, V.; Lavagna, M.; Bevilacqua, R. Stereovision-based pose and inertia estimation of unknown and uncooperative space objects. *Adv. Space Res.* **2017**, *59*, 236–251. [CrossRef]
21. Subbarao, K.; Welsh, S. Nonlinear control of motion synchronization for satellite proximity operations. *J. Guid. Control Dyn.* **2008**, *31*, 1284–1294. [CrossRef]
22. Alex Pothen, A.; Crain, A.; Ulrich, S. Pose tracking control for spacecraft proximity operations using the Udwadia–Kalaba framework. *J. Guid. Control Dyn.* **2022**, *45*, 296–309.
23. Di Mauro, G.; Schlotterer, M.; Theil, S.; Lavagna, M. Nonlinear control for proximity operations based on differential algebra. *J. Guid. Control Dyn.* **2015**, *38*, 2173–2187. [CrossRef]
24. Sun, L.; Huo, W. Robust adaptive backstepping control for autonomous spacecraft proximity maneuvers. *Int. J. Control Autom. Syst.* **2016**, *14*, 753–762. [CrossRef]
25. Gui, H.; de Ruiter, A.H.J. Adaptive fault-tolerant spacecraft pose tracking with control allocation. *IEEE Trans. Control Syst. Technol.* **2019**, *27*, 479–494.
26. Wang, Y.; Liu, K.; Ji, H. Adaptive robust fault-tolerant control scheme for spacecraft proximity operations under external disturbances and input saturation. *Nonlinear Dyn.* **2022**, *108*, 207–222. [CrossRef]
27. Lee, D. Nonlinear disturbance observer-based robust control of attitude tracking of rigid spacecraft. *Nonlinear Dyn.* **2017**, *88*, 1317–1328. [CrossRef]
28. Fu, J.; Chen, L.; Zhang, D.; Zhang, J.; Shao, X. Disturbance observer-based prescribed performance predictive control for spacecraft on-orbit inspection. *J. Guid. Control Dyn.* **2022**, *45*, 1873–1889. [CrossRef]
29. Dong, H.; Hu, Q.; Akella, M.R.; Mazenc, F. Partial Lyapunov strictification: Dual-quaternion-based observer for 6-DOF tracking control. *IEEE Trans. Control Syst. Technol.* **2019**, *27*, 2453–2469. [CrossRef]
30. Sun, G.; Zhou, M.; Jiang, X. Non-cooperative spacecraft proximity control considering target behavior uncertainty. *Astrodynamics* **2022**, *6*, 399–411. [CrossRef]
31. Zhang, L.; Xia, Y.; Shen, G.; Cui, B. Fixed-time attitude tracking control for spacecraft based on a fixed-time extended state observer. *Sci. China Inf. Sci.* **2021**, *64*, 212201. [CrossRef]
32. Wang, K.; Meng, T.; Wang, W.; Song, R.; Jin, Z. Finite-time extended state observer based prescribed performance fault tolerance control for spacecraft proximity operations. *Adv. Space Res.* **2022**, *70*, 1270–1284. [CrossRef]
33. Wang, X.; Wang, Z.; Zhang, Y. Model predictive control to autonomously approach a failed spacecraft. *Int. J. Aerosp. Eng.* **2018**, *2018*, 1–18. [CrossRef]
34. Wang, X.; Li, Y.; Zhang, X.; Zhang, R.; Yang, D. Model predictive control for close-proximity maneuvering of spacecraft with adaptive convexification of collision avoidance constraints. *Adv. Space Res.* **2023**, *71*, 477–491. [CrossRef]
35. Lee, K.; Park, C.; Eun, Y. Real-time collision avoidance maneuvers for spacecraft proximity operations via discrete-time Hamilton–Jacobi theory. *Aerosp. Sci. Technol.* **2018**, *77*, 688–695. [CrossRef]
36. Li, Q.; Gao, D.; Sun, C.; Song, S.; Niu, Z.; Yang, Y. Prescribed performance-based robust inverse optimal control for spacecraft proximity operations with safety concern. *Aerosp. Sci. Technol.* **2023**, *136*, 108229. [CrossRef]
37. Wang, Y.; Bai, Y.; Xing, J.; Radice, G.; Ni, Q.; Chen, X. Equal-collision-probability-curve method for safe spacecraft close-range proximity maneuvers. *Adv. Space Res.* **2018**, *62*, 2599–2619. [CrossRef]
38. Ikeya, K.; Liu, K.; Girard, A.; Kolmanovsky, I. Learning reference governor for constrained spacecraft rendezvous and proximity maneuvering. *J. Spacecr. Rocket.* **2023**, *60*, 1127–1141. [CrossRef]
39. Dong, H.; Hu, Q.; Akella, M.R. Dual-quaternion-based spacecraft autonomous rendezvous and docking under six-degree-of-freedom motion constraints. *J. Guid. Control Dyn.* **2018**, *41*, 1150–1162. [CrossRef]
40. Yang, J.; Stoll, E. Adaptive sliding mode control for spacecraft proximity operations based on dual quaternions. *J. Guid. Control Dyn.* **2019**, *42*, 2356–2368. [CrossRef]
41. Hamilton, W.R. XI. On quaternions; or on a new system of imaginaries in algebra. *Lond. Edinb. Dublin Philos. Mag. J. Sci.* **1848**, *33*, 58–60. [CrossRef]
42. Clifford. Preliminary sketch of biquaternions. *Proc. Lond. Math. Soc.* **1871**, *S1–S4*, 381–395.
43. Filipe N. Nonlinear Pose Control and Estimation for Space Proximity Operations: An Approach Based on Dual Quaternions. Ph.D. Thesis, Georgia Institute of Technology, Atlanta, GA, USA, 2014.
44. Sullivan, J.; Grimberg, S.; D'Amico, S. Comprehensive survey and assessment of spacecraft relative motion dynamics models. *J. Guid. Control Dyn.* **2017**, *40*, 1837–1859. [CrossRef]
45. Moreno, J.A.; Osorio, M. A Lyapunov approach to second-order sliding mode controllers and observers. In Proceedings of the 2008 47th IEEE Conference on Decision and Control, Cancun, Mexico, 9–11 December 2008; pp. 2856–2861.

46. Moreno, J.A. A linear framework for the robust stability analysis of a generalized super-twisting algorithm. In Proceedings of the 2009 6th International Conference on Electrical Engineering, Computing Science and Automatic Control (CCE), Toluca, México, 10–13 November 2009; pp. 1–6.
47. Li, Q.; Yuan, J.; Zhang, B.; Wang, H. Artificial potential field based robust adaptive control for spacecraft rendezvous and docking under motion constraint. *ISA Trans.* **2019**, *95*, 173–184. [CrossRef]
48. Zhou, H.; Dang, Z.; Zhang, Y.; Yuan, J. Collision-free control of a nano satellite in the vicinity of China Space Station using Lorentz augmented composite artificial potential field. *Acta Astronaut.* **2023**, *203*, 88–102. [CrossRef]
49. Schaub, H.; Junkins, J.L., Gravitational potential field models. In *Analytical Mechanics of Space Systems*, 4th ed.; AIAA Education Series; American Institute of Aeronautics and Astronautics, Inc.: Washington, DC, USA, 2018; Chapter 11, pp. 621–646.
50. Miller, S.; Walker, M. L.; Agolli, J.; Dankanich, J. Survey and performance evaluation of small-satellite propulsion technologies. *J. Spacecr. Rocket.* **2021**, *58*, 222–231. [CrossRef]